Review | Open Access

Micro Nano Science

Ye et al. Micro Nano Sci. 2026, 1, 17 DOI:10.20517/mns.2026.09

Advances on triply periodic hyperbolic surface structures: from biological inspiration to artificial self-assembly

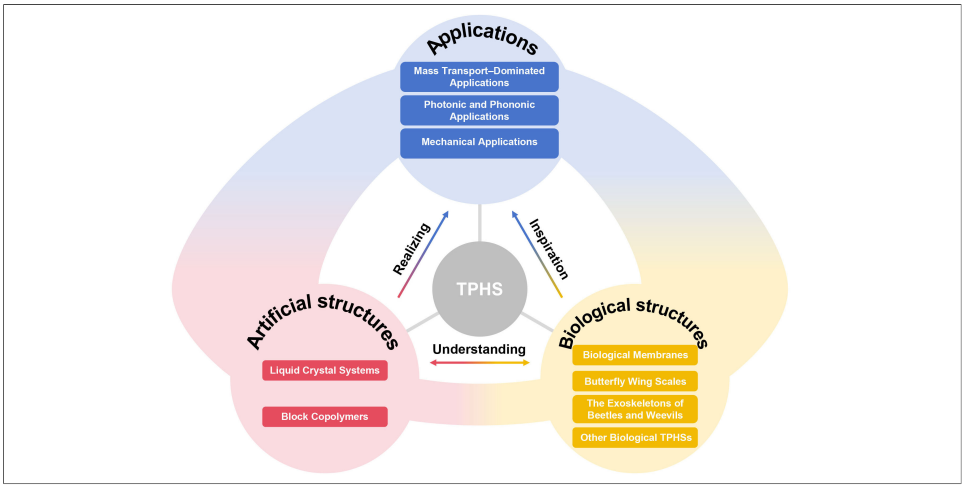
Shuai Ye, Lu Han*

Keywords:
Hyperbolic geometry, mean curvature, Gaussian curvature, self-assembly

Citation: Ye, S.; Han, L. Advances on triply periodic hyperbolic surface structures: from biological inspiration to artificial self-assembly. *Micro Nano Sci.* **2026**, *1*, 17. https://dx.doi.org/10.20517/mns.2026.09

Received: 26 Jul 2026
First Decision: 21 Aug 2026
Revised: 27 Sep 2026
Accepted: 13 Oct 2026
Published: 2 Nov 2026

Academic Editor:
Jing Wei
Copy Editor:
Shu-Yuan Duan
Production Editor:
Shu-Yuan Duan



Abstract

Triply periodic hyperbolic surfaces (TPHSs) are a class of complex structures that extend periodically throughout three-dimensional space and possess smooth surfaces with non-positive Gaussian curvature. They appear in a wide range of natural systems, from cellular membranes to butterfly wing scales and beetle exoskeletons. Owing to their unique geometries and extraordinary properties, TPHSs have attracted extensive attention and research interest. Detailed structural characterizations of naturally occurring TPHSs have been performed, and a variety of artificial analogs have been fabricated by top-down physical methods and bottom-up chemical approaches. These efforts have deepened our understanding of TPHSs and broadened their application scope. This review discusses the progress on TPHSs in biological systems and their artificial synthesis, and it surveys current applications of these structures in fields such as photonics, energy storage and conversion, catalysis, sensing, thermal management and mechanical metamaterials. It thereby provides a new framework linking biological structures to artificial structures. Finally, this review concludes by outlining current challenges and proposing directions for future research.

Check for updates

School of Chemical Science and Engineering, Tongji University, Shanghai 200092, China.

*Correspondence to: Prof. Lu Han, School of Chemical Science and Engineering, Tongji University, Shanghai 200092, China. E-mail: luhan@tongji.edu.cn

INTRODUCTION

Triply periodic hyperbolic surfaces (TPHSs), characterized by their hyperbolic geometry, were introduced by mathematicians and have since evolved into an interdisciplinary field spanning mathematics, physics, chemistry, biology, and engineering. The earliest examples, discovered by Hermann Amandus Schwarz in 1865 and later by his student Edvard Rudolf Neovius in 1883 through solving the Plateau problem and its generalizations, were the Schwarz primitive (P), Schwarz diamond (D), Schwarz hexagonal (H), Schwarz crossed layers of parallels and Neovius (N) surfaces, which revealed triply periodic minimal surfaces (TPMSs) and established the field[1-4]. In 1970, NASA scientist Alan Schoen proposed twelve new TPMSs, among which the gyroid (G) surface has become the most celebrated[5].

TPHSs attract extensive attention owing to their unique geometry, including three-dimensional (3D) periodicity, interconnected channels, high specific surface areas, and most critically, non-positive Gaussian curvature[1,6-10]. Several reviews[1,6,11-19] have discussed their natural occurrences, artificial self-assembly and applications. Recent advances - symmetry-breaking synthesis, curvature-mediated transitions, kinetic control, data-driven structure prediction and curvature-specific functionality - call for a unified framework linking biological morphogenesis with artificial fabrication. This review addresses that gap.

This review first outlines the definition and classification of TPHSs. We then present their structural and functional diversity in natural systems and progress in uncovering their formation mechanisms. Next, we review bottom-up self-assembly based on liquid crystals and block copolymers for fabricating TPHS materials, followed by a summary of their applications [Figure 1]. Finally, we identify gaps between biological mechanisms, artificial design and practical applications, and provide an outlook on cross-scale fabrication and function-oriented design.

STRUCTURAL DESCRIPTIONS

Understanding these structures begins with curvature. The maximum and minimum normal curvatures at a point are the principal curvatures, denoted κ_1 and κ_2[31]. Their product is the Gaussian curvature, K, and their arithmetic mean is the mean curvature, H. When H is constant, the surface is a constant mean curvature (CMC) surface; for TPMSs, $H(p)$ vanishes everywhere and $K(p) \leq 0$[1,31], making TPMSs a special subclass of CMC surfaces. Structures formed by shifting TPMSs along their surface normals by a constant distance are called parallel surfaces[1]. These TPMSs partition space into interpenetrating labyrinthine domains; shifting a TPMS toward one side yields a CMC or parallel surface bounding one labyrinth and producing an unbalanced structure. The labyrinths can be abstracted into skeletal networks of nodes and struts (channel segments), facilitating structural identification[1,13]. Experimentally, self-assembly has produced a variety of these structures. TPMSs are intrinsically balanced and fabricated readily under thermodynamically favorable conditions, whereas CMC and parallel surfaces are typically obtained via reverse-micelle synthesis or kinetically controlled processes that trap them in thermodynamically nonequilibrium states. In this review, TPMSs, CMC surfaces and parallel surfaces are collectively termed TPHSs, characterized by three-dimensionally periodic and smooth surfaces with non-positive Gaussian curvature (saddle-shaped geometry).

The three most common TPMSs - G, D and P - possess the most uniform Gaussian curvature distributions[32]. The G surface with space group $Ia\bar{3}d$ (No. 230) contains no straight lines or mirror planes and divides space into two interpenetrating skeletal networks of three-fold connectivity. These two networks are chiral enantiomers, rendering the overall structure achiral [Figure 2A]. The D surface contains straight lines and two-fold rotation axes, and its space group is $Pn\bar{3}m$ (No. 224). It separates space into two diamond networks with four-fold connectivity [Figure 2B]. The P surface is assigned to the space group $Im\bar{3}m$ (No.

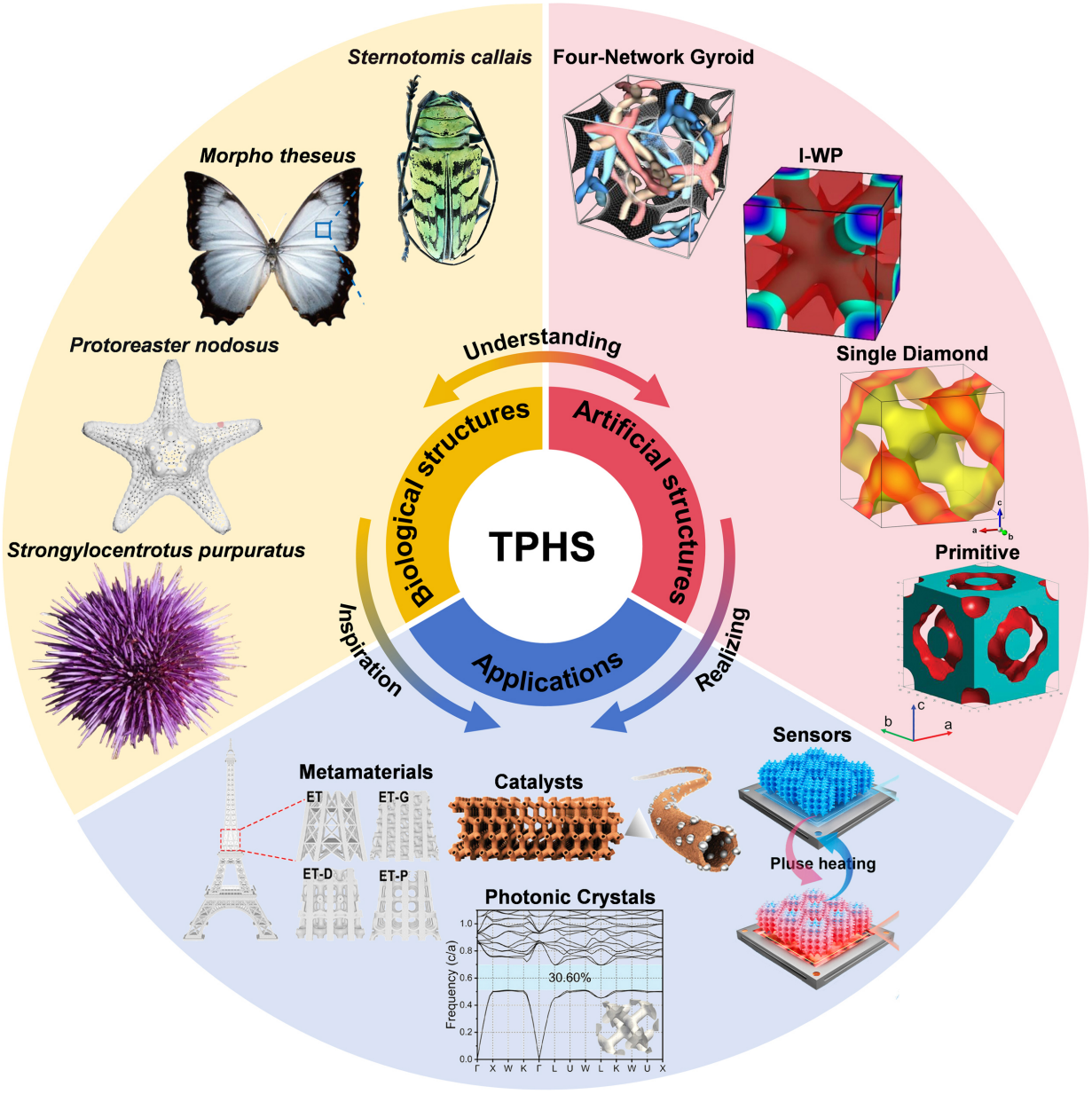


Figure 1. Schematic illustration of research progress on TPHSs in biological structural elucidation, artificial self-assembly systems and related applications. (*Strongylocentrotus purpuratus*) Reproduced under the terms of the CC BY-NC 3.0 License[20]. Copyright 2025, The Authors. (*Protoreaster nodosus*) Reproduced with permission[21]. Copyright 2022, The American Association for the Advancement of Science. (*Morpho theseus*) Reproduced under the terms of the CC BY 4.0 License[22]. Copyright 2023, The Authors. (*Sternotomis callais*) Reproduced with permission[23]. Copyright 2021, The Royal Society. (Four-Network Gyroid) Reproduced under the terms of the CC BY 4.0 License[24]. Copyright 2025, The Authors. (I-WP) Reproduced under the terms of the CC BY-NC 4.0 License[25]. Copyright 2020, The Authors. (Single Diamond) Reproduced under the terms of the CC BY-NC-ND 4.0 License[26]. Copyright 2024, The Authors. (Primitive) Reproduced with permission[27]. Copyright 2024, The American Association for the Advancement of Science. (Sensors) Reproduced under the terms of the CC BY-NC-ND 4.0 License[7]. Copyright 2026, The Authors. (Catalysts) Reproduced under the terms of the CC BY-NC 4.0 License[28]. Copyright 2024, The Authors. (Photonic Crystals) Reproduced with permission[29]. Copyright 2026, Wiley-VCH GmbH. (Metamaterials) Reproduced under the terms of the CC BY 4.0 License[30]. Copyright 2025, The Authors. TPHS: Triply periodic hyperbolic surface; I-WP: I-graph-Wrapped Package graph; ET: Eiffel Tower.

229) and lies between two interlocked simple cubic lattices with six-fold connectivity[1,6,14] [Figure 2C]. Interestingly, due to the complex structure of the P surface, it is also referred to as the "plumber's nightmare"[1,13,34]. These balanced surfaces divide space into two equal-volume labyrinths, and are therefore ordered bicontinuous structures[6,13]. The corresponding double-network structures are also known as double

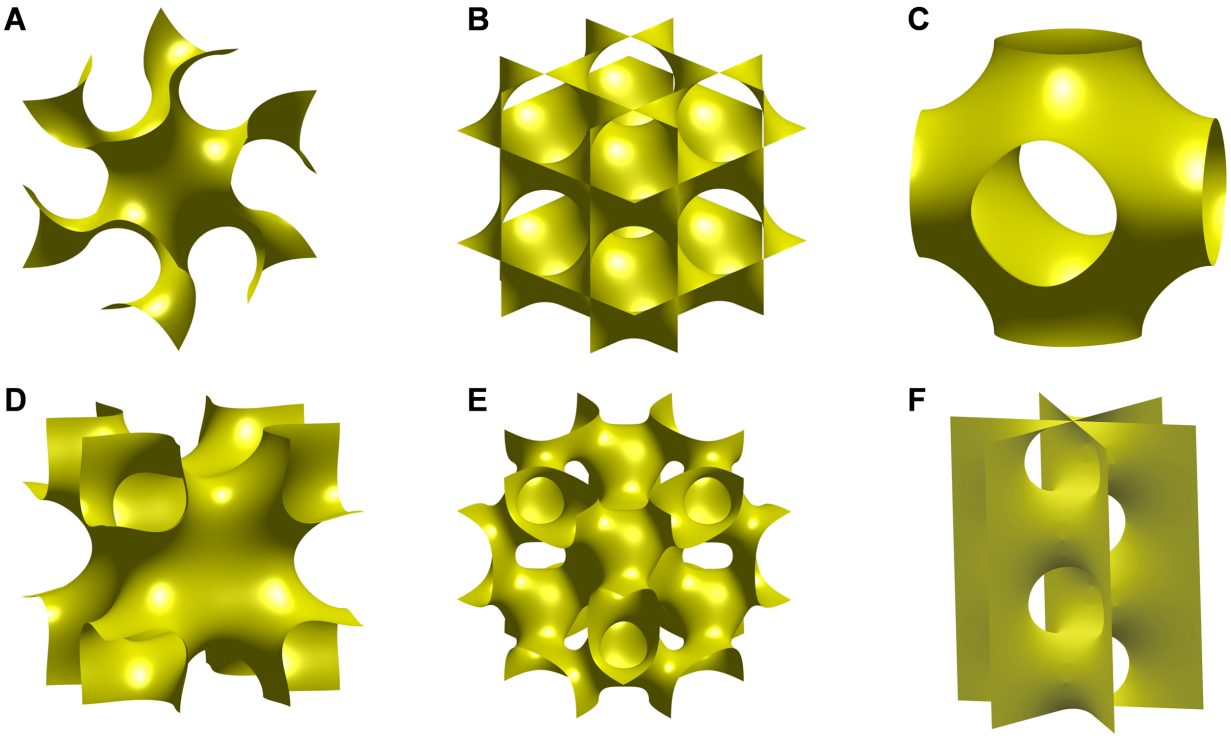


Figure 2. Schematic drawings of TPMSs: (A) G surface; (B) D surface; (C) P surface; (D) I-WP surface; (E) F-RD surface and (F) the branched hexagonal minimal surface. Panels (A-E) were created with MATLAB (R2026a, MathWorks) and panel (F) was created with Surface Evolver[33]. TPMS: Triply periodic minimal surface; I-WP: I-graph-Wrapped Package graph; F-RD: F-graph-Rhombic Dodecahedra graph.

G (DG), double D (DD) and double P (DP), respectively. CMC surfaces are generally unbalanced, dividing space into unequal labyrinths. When only one selected labyrinth is retained as the material-filled phase while the others remain empty, a single-network structure is obtained. The structures derived from the G, D, and P surface geometries through this process are termed single G (SG), single D (SD) and single P (SP), respectively[1,35,36]. SG, SD, and SP adopt space groups $I4_132$ (No. 214), $Fd\bar{3}m$ (No. 227) and $Pm\bar{3}m$ (No. 221), respectively[37]. SG exists in two enantiomeric forms [left-handed (LH) and right-handed (RH)], with chirality arising from the entire periodic network rather than local helical motifs[38]. Compared with double networks, these single-network structures possess lower symmetry, thereby exhibiting altered properties such as photonic bandgaps[1,37,39,40]. When two interlocking double networks shift relative to each other, they produce a family of low-symmetry structures, which are referred to as shifted DG (SDG), shifted DD (SDD) and shifted DP (SDP)[1,14]. These shifted structures create new geometric features and research subjects[8,12,41-44].

The G, D and P surfaces can be interconverted by the theoretical Bonnet transformation, which preserves the intrinsic geometry but cannot occur in real systems because it would require thermodynamically forbidden interpenetration and reorganization. It therefore describes only the geometrical equivalence, not observable phase transitions[1,45]. Schröder-Turk *et al.* calculated the homogeneity of the three surfaces under different length normalizations[46]. For constant surface-to-volume ratio (V/A) or constant average distance function ($\langle d \rangle$, where $d(p)$ is the point-wise channel radius and $\langle d \rangle$ is its average), G is the most homogeneous, with smallest curvature fluctuations (the standard deviation of the distribution of Gaussian curvature, ΔK) and distance-function fluctuations (the standard deviation of the distribution of the channel radius, Δd). For constant average Gaussian curvature ($\langle K \rangle$), G has the smallest Δd, while ΔK is identical among G, D and P due to the Bonnet isometry[46]. Meanwhile, the non-cubic surface families furnish topology-preserving transformation pathways between the three cubic surfaces. These transformations are not Bonnet

Table 1. Comparison of space groups, connectivity and volume fractions of one labyrinth of TPMSs

Surfaces	Space groups	Connectivity	Volume fractions of one labyrinth
G	$Ia\bar{3}d$ (No. 230)	3	0.5
D	$Pn\bar{3}m$ (No. 224)	4	0.5
P	$Im\bar{3}m$ (No. 229)	6	0.5
I-WP	$Im\bar{3}m$ (No. 229)[47]	8	0.536[50]
F-RD	$Fm\bar{3}m$ (No. 225)[5,47]	12	0.532[50]
The branched hexagonal minimal surface	$P6_3/mcm$ (No. 193)[48,49]	3	0.333[48,49]

The two labyrinths of the G, D and P surfaces have equal volume fractions of 0.5. For the I-WP and F-RD surfaces, the values listed in the table are the volume fractions of one of the two labyrinths; the volume fraction of the other labyrinth can be obtained by subtracting the tabulated value from 1. The connectivity values of 8 and 12 also refer to one of the two labyrinths. The branched hexagonal minimal surface divides space into three identical labyrinths; therefore, each labyrinth has a volume fraction of 0.333. TPMS: Triply periodic minimal surface; G: gyroid; D: diamond; P: primitive; I-WP: I-graph-Wrapped Package graph; F-RD: F-graph-Rhombic Dodecahedra graph.

transformations: along these pathways, the free parameters of the surfaces vary continuously. Between D and G lie two pathways: a tetragonal pathway (D → tD → tG → G) and a rhombohedral pathway (D → rPD → P → rPD → rG → G). The tetragonal pathway exhibits higher curvature (smaller ΔK) and packing homogeneity (smaller Δd), as well as a lower energy cost (calculated under the above three length normalizations, with ΔK and Δd as proxies for the curvature and packing terms of a Helfrich-type energy functional, rather than a true free-energy difference). Notably, P is disadvantaged in packing homogeneity: within the rPD family, P is an inflection point of Δd, and along the pathway from P to D within this family, all intermediate structures are more packing-homogeneous than P[46].

Among TPMSs, unbalanced members such as I-WP [Figure 2D] and F-RD [Figure 2E] divide space into two subspaces of unequal volume yet remain bicontinuous, each side forming an independently connected channel network with multiple connectivity[47]. The branched hexagonal minimal surface [Figure 2F] divides space into three independent subspaces, forming a tricontinuous structure[48,49]. The characteristics of these surfaces are summarized in Table 1.

TPHS STRUCTURES IN BIOLOGICAL SYSTEMS

Organisms have evolved diverse TPHS structures that serve distinct functions, regulating or influencing vital activities. Understanding these biological structures reveals the formation mechanisms of complex natural architectures and the intrinsic structure-function relationships, while providing biomimetic inspiration for the development of novel functional materials.

Biological membranes

Biological membranes, typically phospholipid bilayers, can fold into highly ordered cubic membranes, as observed in mitochondria. Pappas *et al.*[51] and Borysko *et al.*[52] were among the first to describe zigzag patterns in certain mitochondria of the giant amoeba *Chaos carolinensis*. Subsequently, Daniels *et al.*[53] systematically demonstrated that starvation induces the formation of these zigzag structures in amoeba mitochondria. Using electron tomography and computer simulations, Deng *et al.*[54,55] first confirmed that the inner mitochondrial membranes of starved *Chaos carolinensis* can form cubic membrane structures of the TPMSs, and correlated these 3D configurations with dietary status and cellular energy adaptation. Mitochondrial membranes in tree shrew photoreceptor cells can fold into multilamellar G-type cubic structures of 8-12 layers[56]. Bykowski *et al.* related the nanomorphology of prolamellar bodies (PLBs) to pigment composition and growth conditions in *Arabidopsis thaliana*[57] and demonstrated that PLB cubic membranes in etiolated angiosperm seedlings (including *Arabidopsis thaliana*, cucumber and maize) are predominantly of D-type structure rather than the hexagonal structure as previously thought[58]. These

studies reveal that cubic membranes are widespread in protists, plants and animals, providing a foundation for understanding membrane structure-function relationships.

Butterfly wing scales

A striking manifestation of TPHSs is their vivid structural colors, most prominent in butterfly wing scales. Saranathan *et al.* used small-angle X-ray scattering (SAXS) to identify the SG structure in five butterfly species from the families Papilionidae and Lycaenidae[40]. Drawing an analogy to the self-assembly of ABC triblock copolymers, they proposed that a core-shell DG forms in which one network is the extracellular space surrounded by the plasma membrane; chitin is selectively deposited there, and after apoptosis, only the SG-structured chitin remains[40]. Early electron microscopy investigations have been instrumental in revealing the intricate photonic architectures in butterfly scales, laying the groundwork for later 3D structural elucidation[59-62]. Because two-dimensional (2D) projected images cannot prove the existence of both enantiomers, Schröder-Turk *et al.* performed 3D electron tomography on *Callophrys rubi*, confirming a structure approximating a parallel surface of SG with space group $I4_132$[63]; both enantiomers were confirmed, with the LH structure dominant, indicating chiral preference during scale formation. In addition, Winter *et al.* found that these micron-scale domains exhibit preferred orientation[64]. Inoue *et al.* statistically analyzed the chirality of SG structures in *Teinopalpus imperialis* and *Parides sesostris* using *Callophrys rubi* as a control: the percentage of LH crystallites is 89% in *Parides sesostris*, higher than the 68% in *Callophrys rubi*, while *Teinopalpus imperialis* displays purely LH SG structures[65]. These findings reveal species-dependent chiral selection, but the underlying mechanisms still require further exploration.

Wilts *et al.*[66] observed that in the butterfly *Erora opisena*, SG crystallite sizes followed a gradient along the long axis and orientations were random relative to the scale normal. This distribution, together with the chiral imbalance, challenged the pre-folding model proposed by Saranathan *et al.*[40]: a single-crystal membrane cannot explain the random orientations, while a polycrystalline membrane cannot account for defect-free single crystals, and the LH and RH SG enantiomers should occur with roughly equal probability. They therefore proposed a co-folding model in which membrane folding and extracellular chitin deposition occur simultaneously; the molecular chirality of chitin may cause the chiral bias, while the tip-to-base crystallite-size gradient suggests a time-dependent assembly constituting a "time-frozen" sequence of developmental stages[66]. By controlling the developmental time points of the butterfly *Parides sesostris* [Figure 3A-F] for observation, Jessop *et al.*[67] fixed samples on day 13 (approximately 70% development) [Figure 3G] and day 15 (approximately 80% development) [Figure 3H and I], observing that the developing SG structure is not a homogeneous extrusion process, but a fibrous network of interwoven nanofibers ~ 25 nm in diameter; the number of fibers gradually increased and the fibers became more entangled near the lower lamina [Figure 3J-M]. This led to a two-stage model: scale cells first secrete and weave nanofibers into a preliminary network, which is then "smoothed" in later stages into the final solid SG; the specific smoothing mechanism remains unclear[67].

The SG geometry endows butterfly wings with vivid structural colors. Although SG is a potential 3D photonic crystal with a complete bandgap (CBG), the low refractive index of chitin prevents a CBG. SG in *Callophrys rubi* exhibits orientation-dependent scattering, and the suppressed iridescence arises from spatial mixing of colors from crystals of multiple orientations[68]. In *Erora opisena*, SG domains correlate moderately with reflectance[69]. The scales of *Morpho theseus* contain a quasi-ordered tubular structure between a purely tubular state and the SG domain, possibly an early state of the G; color mixing makes the scales appear uniformly white[22]. Thayer *et al.* analyzed 312 scale structures from 286 butterfly species, finding that blue structural colors dominate while red is extremely rare; and that 3D photonic crystals (including SGs and inverse opals) show the most restricted color range of 440 to 560 nm[15]. These studies advance our understanding of structure-optical property relationships in butterfly scales, informing optical optimization and biomimetic design.

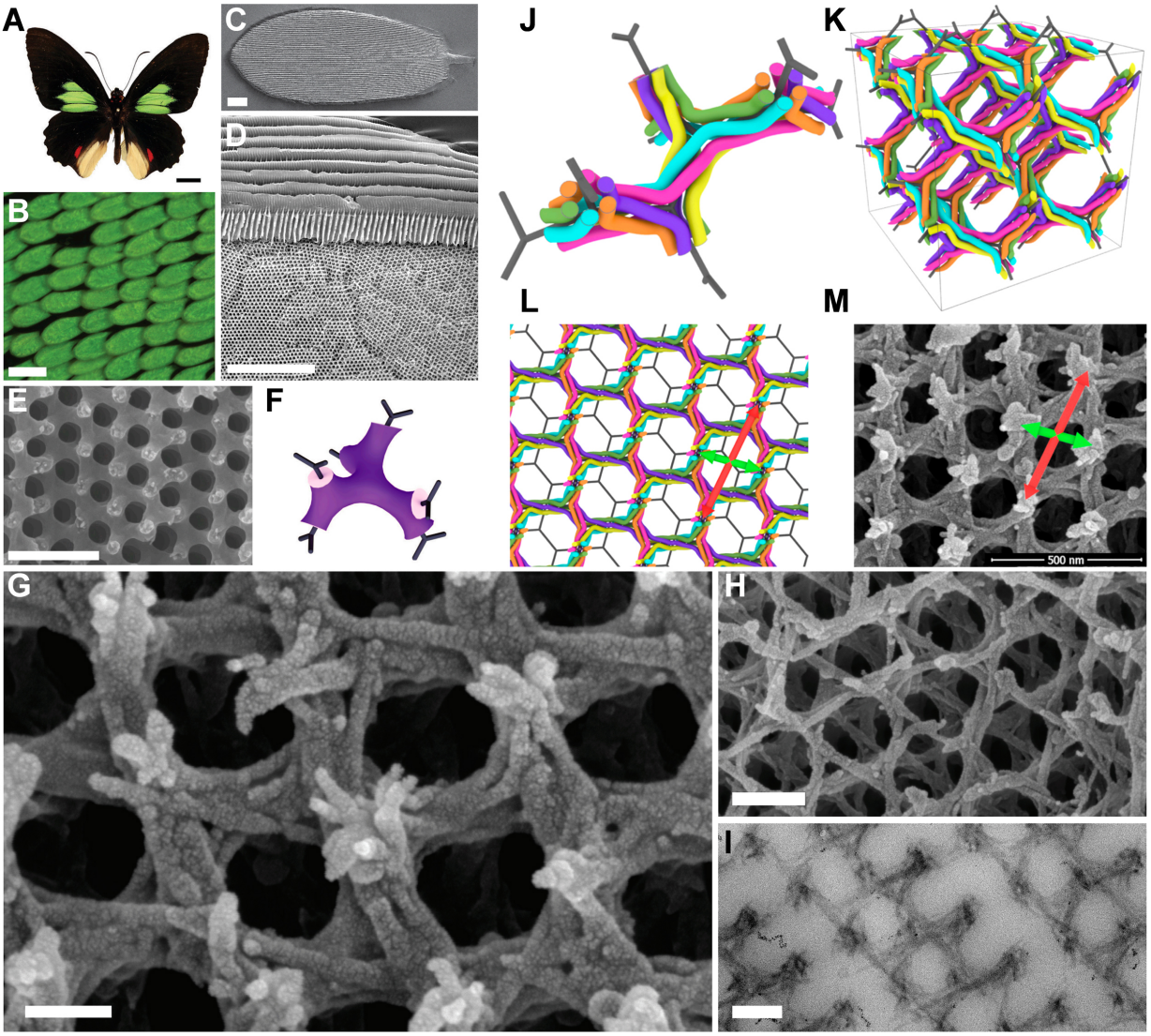


Figure 3. (A-F) SG structure within the green scales of mature *Parides sesostris*. (A) Photograph of a male *Parides sesostris*; (B) Light microscopy image of scales containing the SG structure; (C and D) Scanning electron microscopy (SEM) images of the scales; (E) High-magnification SEM image showing the smooth, homogeneous SG structure; (F) Idealized SG model with a chitin volume fraction of 0.35; (G-I) Electron microscopy images of the fibrillar SG structure in the wing scales of developing *Parides sesostris* pupae. As the pupation period is approximately 18 days, wing scale development was arrested by fixation on day 13 (G, 70% development) and day 15 (H and I, 80% development); (G) Adjacent to the lower lamina of the scale, showing approximately six fibers composing the SG; (H) Adjacent to the upper lamina of the scale, showing 2-3 fibers; (I) Transmission electron microscopy (TEM) image of a cross-section of a scale sampled from the same wing as that shown in (H); (J-M) Geometric model of six helical fibers woven around the SG network; (J) A small section of the model; (K) Approximately 2^3 unit cells; (L) The full six-fiber weave, with the model confined to a thin slice to simulate the finite observation depth of electron microscopy sections; (M) SEM image of the SG structure at 70% development in *Parides sesostris*, showing visual similarity to the model in (L). Scale bars: (A) 1 cm, (B) 100 μm, (C) 10 μm, (D) 5 μm, (E) 500 nm, (G) 100 nm, (H) and (I) 200 nm. This figure is reproduced under the terms of the CC BY-NC-ND 4.0 License[67]. Copyright 2025, The Authors. SG: Single gyroid.

The exoskeletons of beetles and weevils

Coleoptera such as beetles and weevils are another major group that evolved TPHS structures. Bartl *et al.* discovered SD microdomains in the green scales of the weevil *Lamprocyphus augustus*; their multiple orientations enable effective reflection of light from different incident directions[70], highlighting the different optical structural preference between *Lepidoptera* and *Coleoptera*. Wilts *et al.* found that the elytron scales of *Entimus imperialis* are also composed of SD microdomains of different orientations[71]. Although individual microdomains reflect light highly directionally, the scales are densely arranged in concave pits; when light

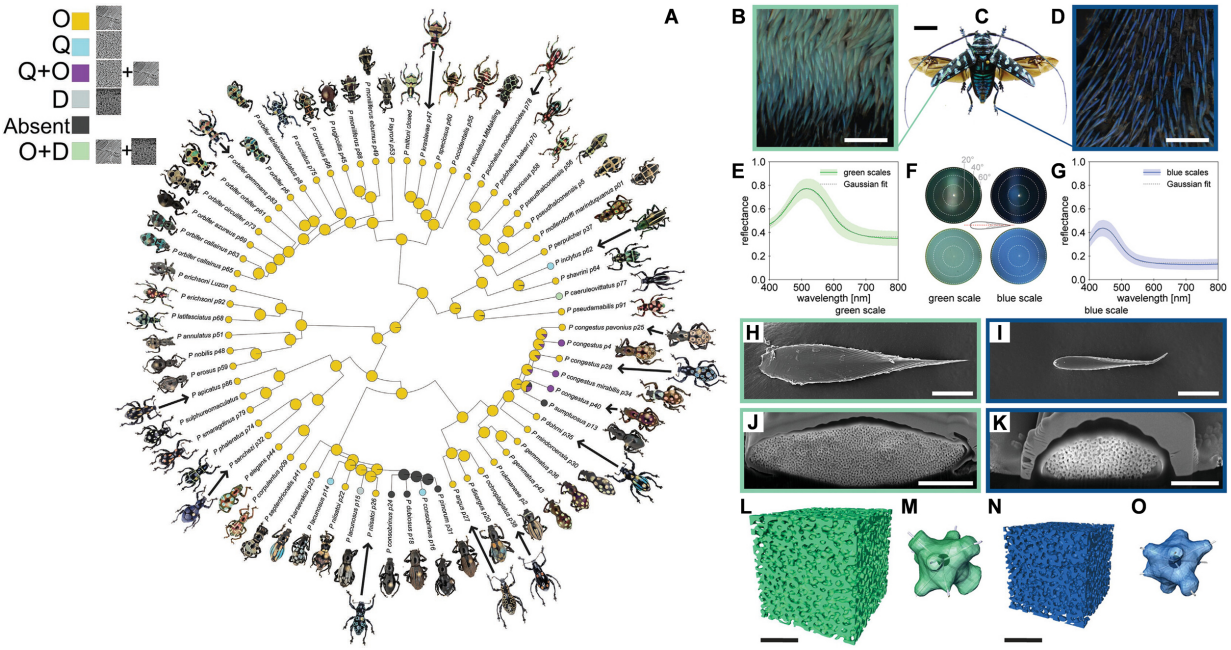


Figure 4. (A) Phylogenetic tree of weevils from the genus *Pachyrhynchus*, showing the evolutionary distribution of photonic crystal structure types within the scales of different species (O, Q, D denote Ordered, Quasi-ordered and Disordered, respectively). (A) Reproduced under the terms of the CC BY-NC 4.0 License[74]. Copyright 2022, The Authors; (B-O) Optical characterization and ultrastructural analysis of the colored scales of *Sternotomis virescens*. (B and D) Reflection light micrographs of green (B) and blue (D) scales. (C) Photograph of a male beetle. (E and G) In situ reflectance spectra of the green (E) and blue (G) scales; (F) K-space images of the two scale colors at 100× magnification. (H and I) SEM images showing the seed-like shape of individual green (H) and blue (I) scales. (J and K) Focused ion beam-SEM cross-sectional images showing that both the green (J) and blue (K) scales are amorphous networks surrounded by a thin-film cortex. (L and N) 3D reconstructed networks of the green (L) and blue (N) scales obtained from focused ion beam-SEM tomography. (M and O) A selected sub-unit from the networks of the green (M) and blue (O) scales. Scale bars: (B) and (D) 125 μm, (C) 1 cm, (H) and (I) 20 μm, (J) 5 μm, (K) 2 μm, (L) and (N) 1 μm. (B-O) Reproduced under the terms of the CC BY-NC 4.0 License[78]. Copyright 2023, The Authors. SEM: Scanning electron microscopy.

from the pit walls and different microdomains spatially overlaps, the reflectance peaks at ~ 540 nm. At close range, weevils distinguish shiny spot patterns for recognition and mating, while from a distance they blend into a green background, evading predators[71]. Wu *et al.* found that the colored and colorless domains of *Entimus imperialis* share the same SD structure. In the colorless domains, the air is replaced by SiO_2, reducing the refractive index contrast with chitin and producing narrow bandgaps[72]. Saranathan *et al.* surveyed ~ 127 arthropod species and found TPHS structures other than SD in beetles, such as SG in *Platyaplastes venustus* and SP in the longhorn beetle *Sternotomis pulchra*; lineage-specific structure preferences may stem from differences in curvature regulation caused by variations in membrane-binding protein expression[73]. In 72 *Pachyrhynchus* weevil species, photonic structures range from long-range order to complete disorder[74] [Figure 4A]. Amorphous D structures can also open photonic bandgaps and produce structural colors[75]. The direct comparison of SD structure and its amorphous counterpart in the red and blue scales of *Pachyrhynchus congestus mirabilis* showed that blue scales lack long-range order yet still open a partial bandgap, demonstrating that long-range order is not necessary for producing structural color[76].

Besides the common G, D and P bio-optical structures, the I-WP surface was also discovered in *Sternotomis callais*[23]. This finding expanded the types of photonic crystals in biology while raising new questions about how cells selectively fill subspaces. For G, D and P structures, the two subspaces can be superimposed via inversion operations or translation, meaning that either can become the extracellular space for chitin filling and the cell does not distinguish them[23]. In contrast, the two subspaces of the I-WP structure have different volume fractions, and the cells always recognize the I-subspace as the extracellular space[23]. Currently, no

specific mechanism has been proposed to explain this phenomenon. Bauernfeind *et al.* studied two longhorn beetle species from the tribe *Sternotomini*, elucidating how polycrystalline to quasi-disordered amorphous I-WP structures produce non-iridescent colors[77,78]. In the green and blue scales of *Sternotomis virescens* [Figure 4B-O], both amorphous I-WP structures have the same volume fraction, but the green-scale struts are longer and thicker (larger periodic size), shifting the reflected peak wavelength; the lack of long-range order causes isotropic scattering, meaning that short-range order provides the color while long-range disorder eliminates iridescence[78]. In *Sternotomis amabilis sylvia*, the green and orange scales correspond to polycrystalline and quasi-disordered I-WP structures, respectively; the flattened scale bases bear transparent distal fins with micrometer-scale ridges that suppress the iridescence of the polycrystalline structure, whereas the quasi-disordered network scatters intrinsically isotropically[77]. These structures have implications for photonic materials design.

Other biological TPHSs

SG structures formed by β-keratin were also discovered in the feathers of *Chloropsis cochinchinensis sensu lato*, showing weak iridescence and saturated blue-green structural colors, representing the first example of directly self-assembled SG crystals known to science[79]. Donnay *et al.* proposed that the interfaces between the organic matrix and inorganic crystals in echinoderm skeletons are TPMSs, which were the first examples reported in nature of periodic minimal surfaces[80]. Subsequently, TPHSs were confirmed in starfish (D)[21,81], sea urchins (SD and SP)[20,82,83] and crinoids (D)[84]; the D structure in the extinct crinoid *Haplocrinites boitardi* pushes the fossil record of TPHSs in biomineralized skeletons back to the Devonian. Unlike the optical roles in butterflies, beetles and birds, the TPHS structure in the knobby starfish *Protoreaster nodosus* primarily exhibits mechanical properties - high stiffness, high strength and high specific energy absorption[21,81,85]. Its skeleton contains a single-crystalline structure with precise crystallographic registration between the atomic-scale calcite and the micrometer-scale D microlattice. The {111} planes of the D microlattice are considered to undergo preferred failure under compression, yet lattice-level dislocations (density 100-1,200 cm^{-2}) generate a "pinning" effect during damage-band propagation, deflecting and constraining the bands. Spatial variations in structural parameters (such as branch length/thickness) and the non-cleavage "conchoidal" fracture of biogenic calcite collectively enhance damage tolerance. The ossicles exhibit non-catastrophic stress plateaus and a specific energy absorption of up to 9.76 $kJ \cdot kg^{-1}$, outperforming many synthetic ceramic and even metallic foams[21]. These studies demonstrate that nature selects TPHSs for their multifunctional properties.

The formation of biological TPHSs reveals four regulatory principles that guide artificial self-assembly. First, chiral selection: butterfly species differ in chiral preference of scale crystallites[64,65]. In artificial systems, molecular chirality enables the chiral blocks to self-assemble into LH and RH SG networks[86,87]. Second, curvature regulation: biological membranes select G, D, P[54,55,73] or I-WP[23] surfaces through a balance among spontaneous curvature, lipid arrangement and the curvature regulation of membrane-binding proteins. Artificial systems tune spontaneous curvature and packing frustration via molecular architecture design[88-93], blending[94-99] and end-group chemistry[27,100]. Third, selective subspace filling: cells recognize and fill the I-subspace in *Sternotomis callais*[23], and chitin is selectively deposited in the extracellular space of butterfly wing scales[40]. Artificial systems achieve this by controlling nucleation-site density to fill one labyrinth of the D surface formed by block copolymers, yielding SD structure[26]. Fourth, dynamic remodeling: *Parides sesostris* forms a woven fibrillar network that later smooths into SG[67]; the random orientations and chiral bias in *Erora opisena* are explained by a co-folding model[66]. Artificial systems regulate this via kinetic pathways such as solvent evaporation rate[101-105], annealing history[106,107], precursor hydrolysis/condensation kinetics[26] and pathway-dependent phase transitions[107,108]. This mapping bridges biological structures and artificial self-assembly. The corresponding synthesis strategies are discussed below.

ARTIFICIAL FABRICATION

Researchers have fabricated TPHSs with controllable structures and functions using artificial methods, including top-down approaches such as additive manufacturing[109-117] and bottom-up strategies based on the self-assembly of block copolymers and liquid crystal systems. This section focuses on bottom-up self-assembly for the construction of TPHS materials.

Across the fabrication strategies below, the final TPHS structure is governed by the interplay of thermodynamic and kinetic control. Under thermodynamic control, the equilibrium phase minimizes the free energy under given molecular and compositional constraints[118,119]. Kinetic control determines which structure is actually accessed under realistic processing conditions, governing nucleation, growth pathways and intermediate states[120,121]. Because TPHS phases are often separated by small free-energy differences and are frequently metastable[122-125], kinetic factors can be decisive.

Liquid crystal systems

Liquid crystals combine the fluid properties of conventional liquids with the ordered characteristics of crystals and are widely regarded as the fourth state of matter[126-129]. They are classified into thermotropic and lyotropic types. Thermotropic liquid crystals undergo a temperature-driven transition from a disordered isotropic phase to an ordered anisotropic phase, as temperature changes alter intermolecular interactions and thus the degree of molecular order and alignment. Lyotropic liquid crystals form ordered mesophases when amphiphilic molecules are dissolved in a solvent at specific concentrations and self-assemble into aggregates or micelles, which further organize into ordered phases[130,131]. Through these two approaches, a rich variety of liquid crystalline phases, including TPHS structures, can be obtained[132-138].

Levelut *et al.* used time-resolved diffraction to confirm the DG structure in thermotropic liquid crystals[139], and Zeng *et al.* reported a triple-network tricontinuous phase based on the P surface[140]. Zeng *et al.* reported the first confirmed DD structure[141], the first SD structure[142], and the second single-network (SP) structure[143] in thermotropic liquid crystal systems. The I-WP[25] [Figure 5A-F] and a tetragonal gyroid with one network twisting synchronously while the other twists randomly[144] were also reported, enriching the library of soft matter self-assembled structures. Chen *et al.*[25], Cao *et al.*[138,144], Cai *et al.*[145] and Cao *et al.*[146] also systematically studied TPHS self-assembly in liquid crystal systems. Using resonant soft X-ray scattering, Cao *et al.* verified two distinct molecular packing modes in DG structures self-assembled from rodlike and taper-shaped molecules: orientation is smoothly transferred through junctions in anisotropic channels filled with aromatic cores, whereas it is mismatched and discontinuous at junctions in isotropic channels filled with alkyl chains[146]. Two intermediate phases (orthorhombic *Fmmm* and hexagonal $P6_3/m$) in the DD-DG transition of bolapolyphiles revealed a stepwise coordination-number change from 4 to 3[145]. An SP → DG → SD alternating single/double network sequence demonstrated that such phases can alternate with continuous changes in molecular structure (e.g., side-chain length), providing ideas for as-yet-unrealized SG-structured liquid crystals[147]. Tang *et al.* reported a four-network gyroid (4NG) with two networks per subspace, discovering a "supertwist" in which the double-helix twist direction opposes the subspace chirality [Figure 5G-O] - challenging the assumption that molecular orientational twist matches network chirality and providing new insight into chiral transfer in liquid crystals[24].

Luzzati *et al.* first resolved a bicontinuous lyotropic G phase in divalent-cation soaps[148,149]. Templer *et al.* systematically investigated the effects of chain length, water content and temperature on the G, D, P and hexagonal phases in a homologous series of 2:1 (mol:mol) saturated fatty acid/phosphatidylcholine mixtures, determining the location and area of the molecular pivotal surface and providing geometric constraints for interfacial-bending energetics[150]. Tang *et al.* revealed the effects of temperature and pressure on the pivotal surface position in the G phase[151]. Vacklin *et al.*[152], Tang *et al.*[153], Shearman *et al.*[154], Tyler *et al.*[155], Barriga

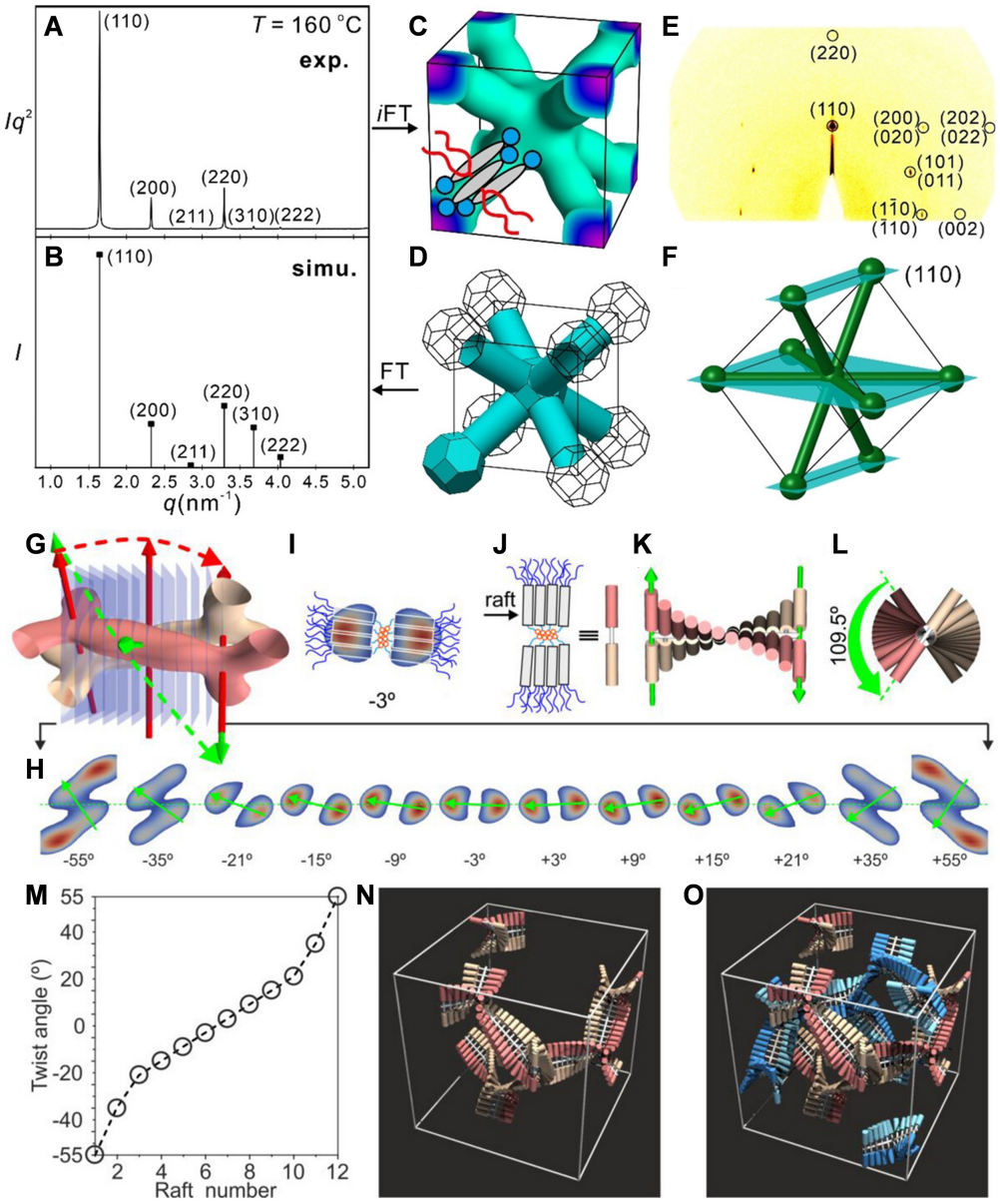


Figure 5. (A-F) SAXS/grazing-incidence SAXS (GISAXS) analysis and structural model of the body-centered cubic phase based on the I-WP minimal surface. (A and B) Experimental (A) and simulated (B) SAXS powder diffractograms; (C) Electron density map reconstructed from (A); (D) Geometric model used to calculate diffraction intensities; (E) Experimental GISAXS pattern, with the [110] axis perpendicular to the substrate; (F) Model of the infinite networks in an $Im\bar{3}m$ unit cell intersected by horizontal (110) planes. (A-F) Reproduced under the terms of the CC BY-NC 4.0 License[25]. Copyright 2020, The Authors; (G-O) Electron density slices of the double-helical segments in the 4NG phase and the supertwist model. (G) Slices of the two strands of a segment of the LH network. The green dashed line traces the 109.5° twist of the molecules between the junctions. The red dashed line traces the twist of the network itself, defined by the -70.5° dihedral angle between the junctions (red arrows). (H) Twelve slices from (G), showing high-electron-density regions; the small green arrows connecting the two electron density maxima define the azimuthal angle, listed below each slice. The change in azimuthal angle between rafts gives the twist angle of the molecules. (I) A schematic molecular structure superimposed on the -3° slice. (J) The model simplified to a dumbbell for tracing the trajectory of each chain in 3D space. (K) Molecular supertwists forming a DG segment between two three-way junctions. (L) Top view of the supertwisted segment. (M) Line plot of azimuthal angle versus slice number, showing the variation of azimuthal angle along the segment. (N) Dumbbell model of the unit cell, showing two interwoven networks. (O) Full four-network model. (G-O) Reproduced under the terms of the CC BY 4.0 License[24]. Copyright 2025, The Authors. SAXS: Small-angle X-ray scattering; DG: double gyroid; 4NG: four-network gyroid; LH: left-handed; I-WP: I-graph-Wrapped Package graph; 3D: three dimensional.

et al.[156] and Kulkarni *et al.*[157] explored the phase stability and lattice parameter modulation through packing frustration energy, lipid chain geometry, thermodynamic conditions and chemical/physical synergistic regulation[152-157]. Pressure-jump time-resolved SAXS and cryo-electron microscopy identified interlamellar

attachments (ILAs) as a key intermediate in the lamellar to cubic transition[158,159]. Van 't Hag *et al.* reviewed the influence of over 130 additives on bicontinuous cubic phases. These strategies overcome the compositional limitations of binary systems and facilitate membrane protein crystallization and drug delivery[160].

Lyotropic liquid crystal structures can be replicated by inorganic precursors, which may overcome soft-matter limitations and realize TPHS structures that are difficult to achieve in pure lyotropic liquid crystal systems. Gao *et al.* synthesized DD mesoporous silica AMS-10 using an anionic surfactant, an organosilane co-structure-directing agent and a silica precursor; adjusting the ionization degree of surfactant headgroup drove a structural evolution from tetragonal $P4_2/mnm$ (cage type, AMS-9), cubic $Fd\bar{3}m$ (cage type, AMS-8), 2D hexagonal $p6mm$ (cylindrical, AMS-3) to cubic $Pn\bar{3}m$ (DD, AMS-10)[161]. Han *et al.* utilized cationic surfactants with bulky polar headgroups and hydrophobic side chains attached near the headgroup to build a mesoporous material whose silica pore wall follows a hexagonal minimal surface; varying ammonia and surfactant concentrations produced a structural evolution from a bicontinuous cubic phase (G) to a tricontinuous structure (the branched hexagonal minimal surface) and then to a 2D hexagonal phase within one templating system[48], validating previous theoretical predictions[49]. The tricontinuous branched hexagonal minimal surface was later also discovered in lyotropic liquid crystals[162].

Block copolymers

Thanks to their highly flexible structural design, block copolymers enable ordered mesostructures through microphase separation driven by entropy and enthalpy. Block incompatibility is described by the Flory-Huggins interaction parameter χ, while χN (where N is the degree of polymerization) represents the driving force for microphase separation. The standard mean-field theory model of ideal symmetric diblock copolymer melts ($f = 0.5$) assumes incompressibility, Gaussian chain statistics, monodispersity, conformational symmetry, negligible fluctuations and a single composition-independent Flory-Huggins interaction parameter. When χN exceeds the critical value of 10.495, the system enters an ordered state[163-166]. However, in real experiments, fluctuations near the order-disorder transition shift the actual transition point from this mean-field prediction[167]. The phases can be controlled by composition, volume fraction and χN[121,168-171]. According to self-consistent field theory (SCFT) and experiments, the G phase in diblock copolymer melts is stable only within a narrow window between the lamellar and hexagonally packed cylindrical phases[172-174]. This window narrows with increasing segregation strength (χN) but can be significantly broadened by conformational asymmetry. G formation is kinetically sensitive to thermal history and annealing conditions - solvent casting or short-time high-temperature annealing tends to produce kinetically trapped metastable states rather than the equilibrium G phase[172-175].

In linear neat diblock copolymer systems, DG is consistently the thermodynamically favored network structure over DD and DP. This has been attributed to the higher node connectivity of DD and DP, which increases packing frustration and chain stretching. Using medial strong segregation (mSST) theory and SCFT, Dimitriyev *et al.* further attributed DG stability to its terminal-boundary geometry: the tubular medial surface of DG is a single twisted sheet without interior corners, allowing chain ends to spread over web-like surfaces and reducing the entropic penalty[124], whereas that of DD and DP possesses multiple leaves intersecting at abrupt angles, tilting and extending the chains and sharply varying the interfacial curvature[124]. They also pointed out that in conformationally symmetric linear diblock copolymers, cubic DD is not metastable but resides at a saddle point, enabling continuous transitions to DG or the T^{111} phase, whereas mSST and SCFT show that homopolymer doping or conformational asymmetry can render DD metastable - fundamentally revising the understanding of DD stability[125]. Lai *et al.*, using polymeric SCFT, predicted that binary blends of homopolymer-like linear diblock copolymers ($f_A = 0.95$) with gyroid-forming linear diblock copolymers stabilize metastable DD and P phases over a broader composition window

through segregation toward node centers and local segregation[176]. Hou *et al.*, using SCFT, first obtained DG, DD and DP simultaneously in pure AB-type block copolymers with the A′(A″B)$_5$ miktoarm star architecture, which combines enhanced spontaneous curvature, combinatorial entropy and local segregation to satisfy the geometric requirements of these networks[88]. Single-network structures (SG, SD and SP) are harder to stabilize: in linear AB diblock copolymers, they are all metastable, tending to reduce domain sizes to maintain a CMC interface and thereby increasing interfacial area per unit volume and the enthalpic penalty[123]. Park *et al.* predicted that SG can be stabilized in H-shaped (BA)$_2$A(AB)$_2$ block copolymers when the A backbone and A arm block sizes are moderately asymmetric[93]. Xie *et al.*[89] and Cheng *et al.*[90] designed a B$_1$AB$_2$AB$_3$ linear pentablock copolymer in which the middle B$_2$ block pushes the longer B$_3$ segment away from the interface via a loop configuration (rather than the previously believed bridging configuration), together with the shorter terminal B$_1$ segment, relieving packing frustration in the matrix and achieving stable SG. Xie *et al.*, using an inverse design algorithm based on the adjoint solution of sequence-SCFT with automatic differentiation and negative selection, calculated that forming the SG with the space group $I2_13$ (a lower symmetry variant of $I4_132$) and the P-like cubic network with the space group $P\bar{4}3n$ requires at least three and ten linear blocks, respectively[177].

Various processing strategies and molecular designs have stabilized different TPHS structures in pure block copolymer systems. Alward *et al.*[178], Thomas *et al.*[179] and Kinning *et al.*[180] first reported an ordered bicontinuous double-diamond (OBDD) phase in poly(styrene-isoprene) (PS-*b*-PI) star block copolymers. Hajduk *et al.* discovered another equilibrium phase in linear PS-*b*-PI, in which the minority component (PS) forms two three-fold-jointed networks, and the majority component (PI) serves as the G matrix[175]. Later calculations revealed that OBDD is metastable under the standard model of linear diblock copolymers[181,182], and it was subsequently revised as a G structure[183]. Susca *et al.* prepared large-size DG single-crystal thick films via evaporation-induced self-assembly (EISA), co-assembling poly(isoprene)-*b*-poly(styrene)-*b*-poly(dimethylaminoethylmethacrylate) (PI-*b*-PS-*b*-PDMAEMA) with poly(methyl vinyl silazane) (PMVS) to obtain single-crystal regions up to 14 mm^2 and over 100 μm thick, pyrolyzable into mesoporous silicon (oxy)nitride monoliths[184]. Lin *et al.*[185] and Chu *et al.*[186-188] stabilized the DD phase using the helical conformations of stereoregular syndiotactic polypropylene (sPP) and isotactic polypropylene (iPP) chains, confirming that configurational regularity is the key to stabilization. Fourier transform infrared (FTIR) spectra revealed that the stabilization originates from stretching-induced helical segments at the nodes rather than ordered packing, with polydispersity acting synergistically[185,186]: a broad chain length distribution alleviates the entropic penalty of packing frustration, while helical conformations and the enthalpy of their associations further compensate it[185]. Adding homopolymer h-sPP broadens the stable temperature window of DD, but upon heating it transforms into a hexagonally packed cylindrical phase rather than DG, via the reorganization of four-arm nodes and end-fusion[95]. In non-stereoregular flexible systems, blending with homopolymers or polymers of different chain lengths is also an effective route to the DD phase[96-99,189].

All of the above-mentioned structures are balanced. To synthesize unbalanced single-network phases, especially analogs of the CMC surfaces found in nature, one strategy is to employ triblock copolymers to form an alternating G (G^A) structure. Dolan *et al.* prepared G^A thin films from polyisoprene-*b*-polystyrene-*b*-poly(ethylene oxide) (PI-*b*-PS-*b*-PEO) via solvent vapor annealing (SVA); *in situ* grazing-incidence SAXS (GISAXS) showed that SVA proceeds through eight distinct stages and that the ternary triblock copolymer exhibits strong robustness to SVA parameters, which is promising for large-area ordered structures[103]. Wang *et al.* employed two chiral triblock terpolymers, polyisoprene-*b*-polystyrene-*b*-poly(L-lactide) (PI-*b*-PS-*b*-PLLA) and polyisoprene-*b*-polystyrene-*b*-poly(D-lactide) (PI-*b*-PS-*b*-PDLA), achieving controlled network chirality in the G^A phase: PLLA and PDLA form LH and RH SG networks, respectively, transferring chirality from the monomeric molecular configuration to the multichain domain morphology. The achiral control sample polyisoprene-*b*-polystyrene-*b*-poly(D,L-lactide) (PI-*b*-PS-*b*-PLA) formed an alternating diamond (D

^{A}) structure[86] [Figure 6A-N]. Another approach to achieving lower symmetry is to shift the networks. Hsueh *et al.* used the DG-forming PS-*b*-PLLA as a template[190]: after removing PLLA, silica precursors were infiltrated to obtain PS/SiO_2 nanohybrids; thermal treatment above the PS glass-transition temperature rearranged the two SiO_2 networks, and subsequent calcination released constraint, allowing more extensive random shifting that broke the inversion symmetry of DG and produced two incoherent SG networks[190].

Compared with G, synthesizing D and P surfaces is considerably more challenging. La *et al.*[91], Ha *et al.*[92] and An *et al.*[191] demonstrated that tuning the molecular design of branched block copolymers and the hydrophilic/hydrophobic molecular-weight ratio can drive the packing parameter above unity, enabling direct self-assembly of G, D and P cubosomes in dilute solution: the bulky branched hydrophilic block limits hydrophobic-chain stretching, increasing the packing parameter. Building on this, cosolvent regulation and blending enable precise, continuous tuning of the P → D → hexagonal phase transitions[91,92,94,191-193]. Lin *et al.* also achieved D and P cubosomes using a linear polystyrene-*b*-poly(ethylene oxide) (PS-*b*-PEO, SEO) diblock copolymer in a dioxane/dimethylformamide mixed solvent at a high initial concentration, where water addition drives self-assembly through hydrophobic interactions of PS chains, and the high initial concentration and high hydrophobic volume fraction synergistically elevate the packing parameter[102]. Lee *et al.* reported the first thermodynamically stable P structure in pure block copolymers: introducing diphosphonic acid linked via an ether bond at the PEO terminus of SEO regulates end-group hydrogen bonding [Figure 6O], inducing "medial packing" in which PEO chain ends aggregate at the microdomain center rather than undergoing skeletal aggregation, alleviating the higher packing frustration of P relative to DD. During cooling after annealing, PEO crystallization merges two three-arm nodes into one six-arm node. If the interaction is too strong (e.g., electrostatic interactions from amine-linked diphosphonic acid), the PEO ends cannot form medial packing or adjust to curvature requirements, preserving the initial curvature[27] [Figure 6P].

Introducing inorganic precursors into the solution self-assembly of block copolymers significantly enhances the structural diversity and properties of TPHS materials. Wiesner has made pioneering contributions to this field. Finnefrock *et al.*[194,195] and Toombes *et al.*[196] utilized poly(isoprene-*b*-ethylene oxide) (PI-*b*-PEO) with (3-glycidyloxypropyl)-trimethoxysilane (GLYMO) and aluminum sec-butoxide to prepare mesoporous aluminosilicates via solvent casting-induced self-assembly. After symmetry breaking was taken into account, the true structure was a DG severely distorted by uniaxial contraction. Inorganic precursors can also yield SG materials: they co-assemble with the triblock terpolymer into a G^{A} structure, are selectively enriched within one block, and after calcination leave one set of inorganic networks[197,198]. Han *et al.* first directly prepared SDD-structured macroporous silica using a triblock copolymer template [poly(tert-butyl acrylate)-*b*-polystyrene-*b*-poly(ethylene oxide) (PtBA-*b*-PS-*b*-PEO)] and tetraethyl orthosilicate (TEOS), which exhibited structural color but no CBG, owing to the low refractive index of silica[43]. Replacing the inorganic source with titanium diisopropoxide bis(acetylacetonate) (TIA) and using a dinonylphenyl end-capped polyethylene glycol-*b*-polystyrene (DNPE-PEO-*b*-PS) template yielded SDD-structured titania whose high dielectric contrast was calculated to open a CBG[42]. In these co-assembly systems, epitaxial intergrowth relationships between SDD and SG, SDP and SDD, and lamellar and SDD structures were observed[41,199,200], and a transition from a 2D cylindrical phase through SG to SDD was found, with SG as a metastable intermediate phase resembling the growth of SG in butterfly wing scales rather than a node-rearrangement transition (no five-fold junctions during the cylinder-to-G transition were observed)[201,202]. Before 2021, SD self-assembly had been reported only in thermotropic liquid crystals[142]. Sheng *et al.* achieved the first direct SD synthesis in block copolymers using a triblock copolymer [poly(ethylene oxide)-*b*-polystyrene-*b*-poly(L-lactide) (PEO-*b*-PS-*b*-PLLA)] with TEOS and explored its epitaxial intergrowth relationships with DD and SG, and the curvature-driven transition[203]. DD and SD share crystallographic directions (such as ⟨111⟩ and ⟨001⟩), while SD and SG connect side by side via the common {121} lattice plane, with unit cell parameters

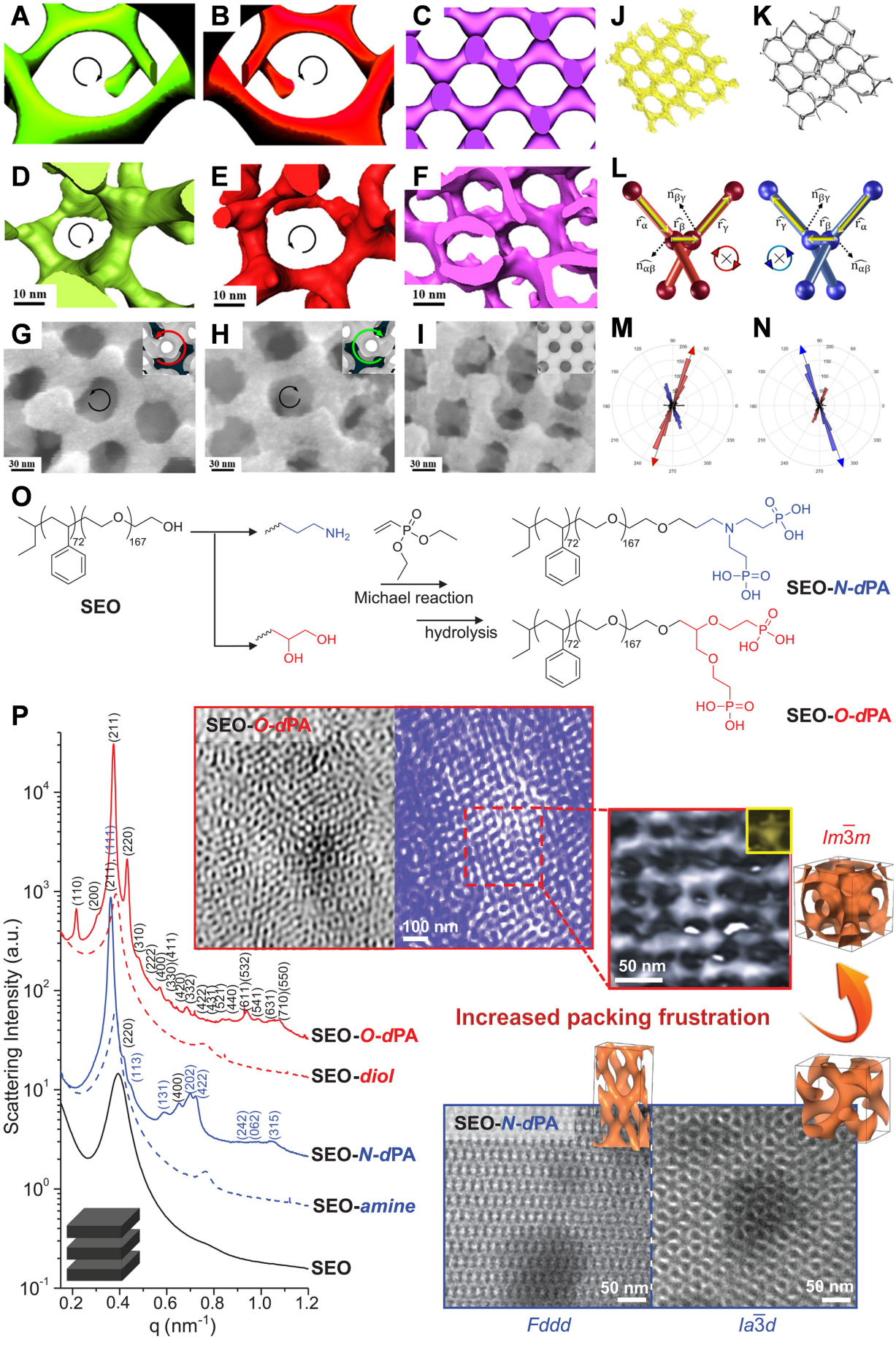


Figure 6. (A-F) 3D imaging of the PI network in self-assembled polylactide-based triblock terpolymers. Simulated images (A-C) and 3D

reconstructions (D-F) from electron tomography of PI-*b*-PS-*b*-PLLA (A and D), PI-*b*-PS-*b*-PDLA (B and E) and PI-*b*-PS-*b*-PLA (C and F), respectively; (G-I) SEM images of the Ni network obtained by templating the polylactide network in PI-*b*-PS-*b*-PLLA (G), PI-*b*-PS-*b*-PDLA (H) and PI-*b*-PS-*b*-PLA (I), respectively; (J-N) Torsion angle analysis of the PI networks based on electron tomography. (J) Reconstructed image of the LH PI network in the G^A phase of self-assembled PI-*b*-PS-*b*-PDLA. (K) Extracted skeleton of (J) by mesh contraction and pruning process. (L) The definition of torsion angle in the G networks for positive chirality (RH, red) and negative chirality (LH, blue). The yellow arrows indicate the vectors of three consecutive edges. (M and N) The polar histograms of torsion angle distribution for the PI network in PI-*b*-PS-*b*-PLLA (M) and PI-*b*-PS-*b*-PDLA (N). The red and blue arrows indicate the torsion angles for ideal G networks formed by PI. (A-N) Reproduced under the terms of the CC BY-NC 4.0 License[86]. Copyright 2020, The Authors; (O and P) Stabilization of different network structures using di-end-functionalized block copolymers. (O) Synthetic routes for the preparation of SEOs having diphosphonic acid (*d*PA) end groups. (P) SAXS profiles of end-functionalized SEOs measured at 25 °C; the dotted SAXS profiles show the morphologies of the end-functionalized block copolymer intermediates. Bright-field TEM images of SEOs-*N*-*d*PA are shown (bottom insets), and tomography images along with a captured TEM image of SEOs-*O*-*d*PA are shown (top insets). (O and P) Reproduced with permission[27]. Copyright 2024, The American Association for the Advancement of Science. SEO: polystyrene-*b*-poly(ethylene oxide); SEO-*O*-*d*PA: *d*PA-ended SEOs (ether linker); SEO-*N*-*d*PA: *d*PA-ended SEOs (amine linker); PI-*b*-PS-*b*-PLLA: polyisoprene-*b*-polystyrene-*b*-poly(L-lactide); PI-*b*-PS-*b*-PDLA: polyisoprene-*b*-polystyrene-*b*-poly(D-lactide); PI-*b*-PS-*b*-PLA: polyisoprene-*b*-polystyrene-*b*-poly(D,L-lactide); G: gyroid; PI: polyisoprene; SAXS: small-angle X-ray scattering; TEM: transmission electron microscopy; 3D: three-dimensional.

satisfying a_{SD}:$a_{SG} \approx 1{:}1.2$, close to the theoretical 1.225; this lattice matching lowers the transition energy barrier, allowing metastable SD to exist locally with DD or SG support[203]. Experiments confirmed that at the boundary between SD and SG, the four-fold nodes gradually transform into three-fold nodes, although SD remained a minor phase with SDD dominant[203]. Subsequently, Wang *et al.* reported a pure SD titania with a CBG[26] [Figure 7] - the first one-pot synthesis of pure SD in block copolymers. PS-*b*-PEO (f_{PEO} = 6.9%) was used as a template to form the D structure in a tetrahydrofuran/hydrochloric acid mixed solvent under thermodynamic control, with PS forming the D surface, and PEO forming two sets of channels for titania deposition[26]. High hydrochloric acid content accelerated TIA hydrolysis and condensation, giving dense nucleation sites that filled both channels (DD); sufficiently low acid content gave sparse nucleation sites, allowing titania to grow in only one set of PEO channels (SD). Photonic bandgap calculations showed a CBG with a bandwidth of 11.54%, but reaching the visible range would require expanding the unit cell parameter to 240 nm[26]. Nonetheless, TiO_2 undergoes pronounced volume shrinkage during the calcination-crystallization process, posing a considerable challenge.

Karpov *et al.*[204] and Djeghdi *et al.*[205] used polyisoprene-*b*-polystyrene-*b*-poly(glycidyl methacrylate) (PI-*b*-PS-*b*-PGMA) to form the D^A structure and prepared the corresponding SD by selectively removing the PI networks and backfilling the voids with gold. Using ptychographic X-ray computed tomography (PXCT), they reconstructed the 3D gold network; three orthogonal slices matched the theoretical SD model, and vertical shrinkage during film drying made the actual unit cell approximately monoclinic rather than cubic. Defects with topological charges of +1/2 (comet-like) and -1/2 (trefoil-like) were identified at the boundaries between two mismatched grains and at the intersection of three grains, respectively[204]. They originated from inter-grain strain, emerged simultaneously, and jointly balanced the topological charge and strain, maintaining long-range order through local disorder. This study demonstrates that topology-driven self-assembly is an important mechanism for structure formation in soft matter, connecting the topological physics of biological and synthetic systems[204-206].

Cooperative self-assembly of small-molecule surfactants with amphiphilic block copolymers introduces competing electrostatic condensation and volumetric expansion, offering high flexibility for material design and curvature control. For instance, adding stearyltrimethylammonium bromide to the self-assembly of polystyrene-*b*-poly(acrylic acid) (PS-*b*-PAA) produced saddle-shaped hierarchical lamellar phases [Figure 8A-D_3], providing direct evidence for the lamellar-to-bicontinuous phase (cubic G) evolutionary pathway[207]. The saddle-shaped lamella exhibits predominantly negative Gaussian curvature (98% of the surface) and near-zero mean curvature [Figure 8E-H_3], yet retains lamellar stacking, revealing the intermediate phase between lamellar and hyperbolic geometries. Lower cationic surfactant additions introduced an unexpected shifted tG phase: although the cationic surfactant attracts and compresses the PAA chains (reducing the

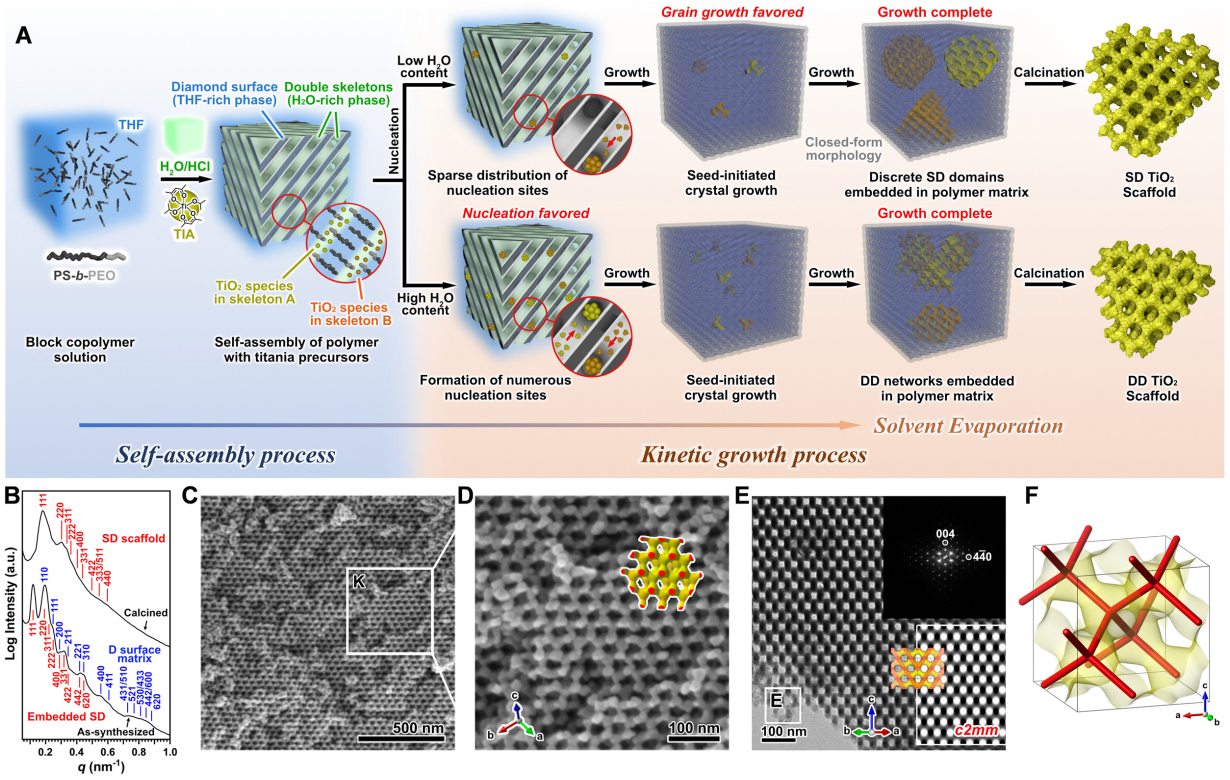


Figure 7. Synthetic strategy and characterization of the SD-structured titania scaffold. (A) The SD-structured titania scaffold was synthesized under dual thermodynamic and kinetic control; by controlling the number of nucleation sites, either DD or SD structures can be formed; (B) SAXS patterns of the as-synthesized and calcined samples; (C and D) Low- and high-magnification SEM images of the calcined SD taken from the {111} plane; (E) TEM image along the [110] direction and the corresponding Fourier diffractogram; (F) The stick model superimposed on the reconstructed volume shows the diamond network with four-fold connectivity. This figure is reproduced under the terms of the CC BY-NC-ND 4.0 License[26]. Copyright 2024, The Authors. THF: Tetrahydrofuran; SD: single diamond; DD: double diamond; PS-*b*-PEO: polystyrene-*b*-poly(ethylene oxide); SAXS: small-angle X-ray scattering; TEM: transmission electron microscopy.

interfacial curvature), the insertion of surfactant micelles into the PAA microdomains increases the hydrophilic block volume (volumetric expansion effect), increasing the interfacial curvature. The balance between these two effects thermodynamically drives the formation of the unique shifted tG structure[208].

For increasingly complex self-assembly systems, data-driven approaches offer new possibilities for phase behavior prediction. For architecturally complex miktoarm star block copolymers (PEO-*s*-PS_2), numerous factors influence their self-assembled structures, making manual structure-parameter analysis difficult. Cui *et al.* constructed a multilayer perceptron (MLP) that learned the self-assembly behavior of PEO-*s*-PS_2 from 802 experimental data points, successfully predicting multi-dimensional synthesis-field diagrams including hyperbolic surface structures[209]. The shape of PEO-*s*-PS_2 resembles that of phospholipid molecules, and its phase behavior provides an ideal model for understanding biological membrane formation[209]. While this data-driven approach enables phase prediction, it does not by itself establish causal mechanisms, which still require independent experimental and theoretical validation[210-212]. Overall, these studies reveal the epitaxial intergrowth transition among TPHS structures, discover various low-symmetry shifted structures (SDD, SDP and shifted tG) and single-network structures (SG, SD). They further combine thermodynamic control with kinetic and curvature regulation and deep learning to achieve phase behavior prediction in complex self-assembly systems.

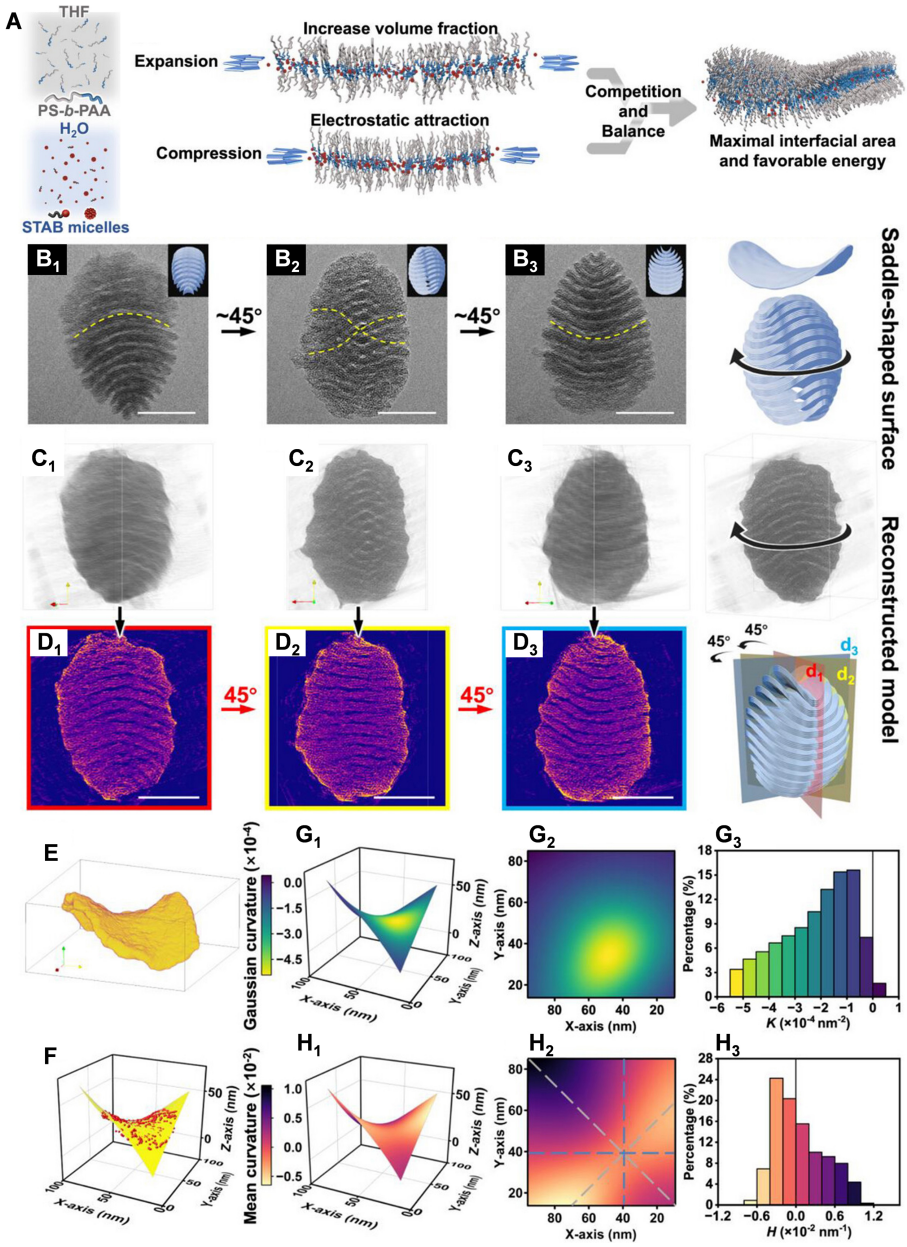


Figure 8. (A) Schematic diagram of the saddle-shaped structure formed by the competition and balance between the electrostatic screening and volume expansion effects; (B_1-B_3) TEM images of the saddle-shaped lamellar phase with secondary multilayer structure. The images were observed from different tilting directions along the long axis of the pupa-like nanoparticles. The corresponding structure model indicates the tilting directions; (C_1-C_3) Different viewpoints of the reconstruction model generated from the 2D TEM image series. The directions of the viewpoints are coincident with those in (B_1-B_3); (D_1-D_3) The corresponding central longitudinal sections obtained from different cross-section directions of the reconstructed model; (E) The single lamella segmented from the reconstructed model; (F) The point cloud extracted from the single lamella and the corresponding fitting surface; (G_1-H_3) The color-coded distributions of *K* (G_1) and *H* (H_1) on the saddle surface, their corresponding planar projections (G_2 and H_2) and histograms of *K* (G_3) and *H* (H_3), respectively. Scale bars: (B_1-B_3) and (D_1-D_3) 100 nm. This figure is reproduced with permission[207]. Copyright 2025, Wiley-VCH GmbH. THF: Tetrahydrofuran; PS-*b*-PAA: polystyrene-*b*-poly(acrylic acid); STAB: stearyltrimethylammonium bromide; TEM: transmission electron microscopy; 2D: two-dimensional.

APPLICATIONS OF TPHS-BASED MATERIALS

TPHS structural materials have been widely applied in fields such as energy storage and conversion[8,213-216], catalysis[217-223], sensors[7,224-230] and others[231-234]. Their functional advantages share three interrelated structural origins. Connectivity and topology effects: the three-dimensionally interconnected channels and

bicontinuous topology allow two non-intersecting labyrinths to accommodate different fluids, reactants or functional components and provide continuous mass transport pathways[6,13,235,236] and a periodic topological basis for wave propagation[237,238]; surface area and pore size effects: the high specific surface area provides abundant active sites, while the tunable mesopore size determines molecular accessibility[239,240], loading capacity[215], and diffusion kinetics[214,215,239]; curvature-specific effects: non-positive Gaussian curvature generates saddle-shaped surfaces, influencing stress distribution (experimental and computational)[30,241-243], defect density (experimental and proposed)[244], the interfacial microenvironment and reaction free energy (computational)[11,245], thereby regulating the mechanical properties and ion adsorption behavior.

Mass transport-dominated applications

The TPHS phases formed by curved lipid bilayers feature two non-intersecting aqueous channels, enabling partitioned drug loading: hydrophilic drugs reside in the aqueous channels, lipophilic drugs in the lipid bilayer, and amphiphilic drugs at the lipid-water interface. Cubosome encapsulation efficiencies can exceed 90% for both small molecules and macromolecules, owing to their extensive internal surface area and tunable lipid composition. The thermodynamic stability of cubosomes preserves structural integrity under physiological conditions. Depending on the formulation, drug release from cubosomes may follow zero-order kinetics or Higuchi diffusion-controlled models, and can be modulated through lipid composition, surface modification or responsive moieties[17,18,236]. Jennings *et al.* constructed a library of 96 lipidoids comprising 8 hydrophilic polyamines and 12 hydrophobic acrylates[246]. They demonstrated two applications: stimuli-responsive thin films formed by interfacial protonation-driven self-assembly that undergo reversible DG ↔ lamellar phase transitions induced by acid, and colloidally stable cubosomes produced by solvent evaporation that retain the internal DG structure and exhibit enhanced membrane fusion, enabling efficient genetic material delivery[246]. Chen *et al.* developed a cubosome-based transdermal system co-loaded with doxorubicin (DOX) and indocyanine green (ICG) (DOX-ICG-cubo) for chemo-photothermal melanoma therapy[247]. The DD-structured cubosomes had a particle size of ~ 101.90 nm and encapsulation efficiencies exceeding 90% for both DOX and ICG, with favorable physiological stability, pH/thermo-dual-responsive release and robust photothermal stability. This system showed synergistic cytotoxicity against B16F10 melanoma cells upon laser irradiation (drug-interaction coefficient < 1) and increased DOX skin permeation to 923.89 ng/cm^2 (enhanced 1.95 times by microneedle pretreatment). In a B16F10 tumor-bearing mouse model, DOX-ICG-cubo gel combined with 808 nm laser irradiation achieved a 97.59% tumor inhibition rate (complete elimination in 3 of 6 mice), outperforming chemotherapy alone (81.41%) and photothermal therapy alone (92.92%), with no obvious toxicity to major organs[247].

TPHS structures feature a 3D continuous and highly ordered pore channel network, which facilitates mass transfer and diffusion of reactants/products and inhibits pore blockage. Their high specific surface area and curved geometry expose more active sites, while the large mesopore size helps expel gas bubbles, synergistically enhancing catalytic activity, selectivity and stability[13,217,248-251]. Wang *et al.* utilized crystalline ordered mesoporous boron phosphate (BPO_4) with an SDD structure as a solid acid catalyst[218]. In the acetalization of furfural with methanol, it achieved > 70% conversion at room temperature within 24 h, with 99.9% selectivity to 2-(dimethoxymethyl)furan, and was reused for 5 cycles without significant loss of activity [Figure 9]. In propane oxidative dehydrogenation, the SDD-structured BPO_4 exhibited higher reaction rates and olefin yields than ordered macroporous BPO_4, reaching 8.70 $g_{olefin}\cdot g_{cat}^{-1}\cdot h^{-1}$ at 540 °C with olefin selectivity above 90%[218]. Li *et al.* used SDD-structured SiO_2 as a hard template for vacuum high-temperature melamine polymerization followed by SiO_2 etching, to replicate an inverse-phased SDD-structured mesoporous graphitic carbon nitride (g-C_3N_4)[217]. Under visible light (λ > 400 nm), it exhibited excellent photocatalytic water splitting with a hydrogen-evolution rate of 6,831 μmol·g^{-1}·h^{-1} - 5 times that of the DG structure and 16 times that of the nonporous control sample, with 90% activity retained after 4 cycles, attributed to enhanced mass transport, bubble release and charge transfer[217]. In electrocatalysis, nitrogen-doped hollow G carbon-Pt

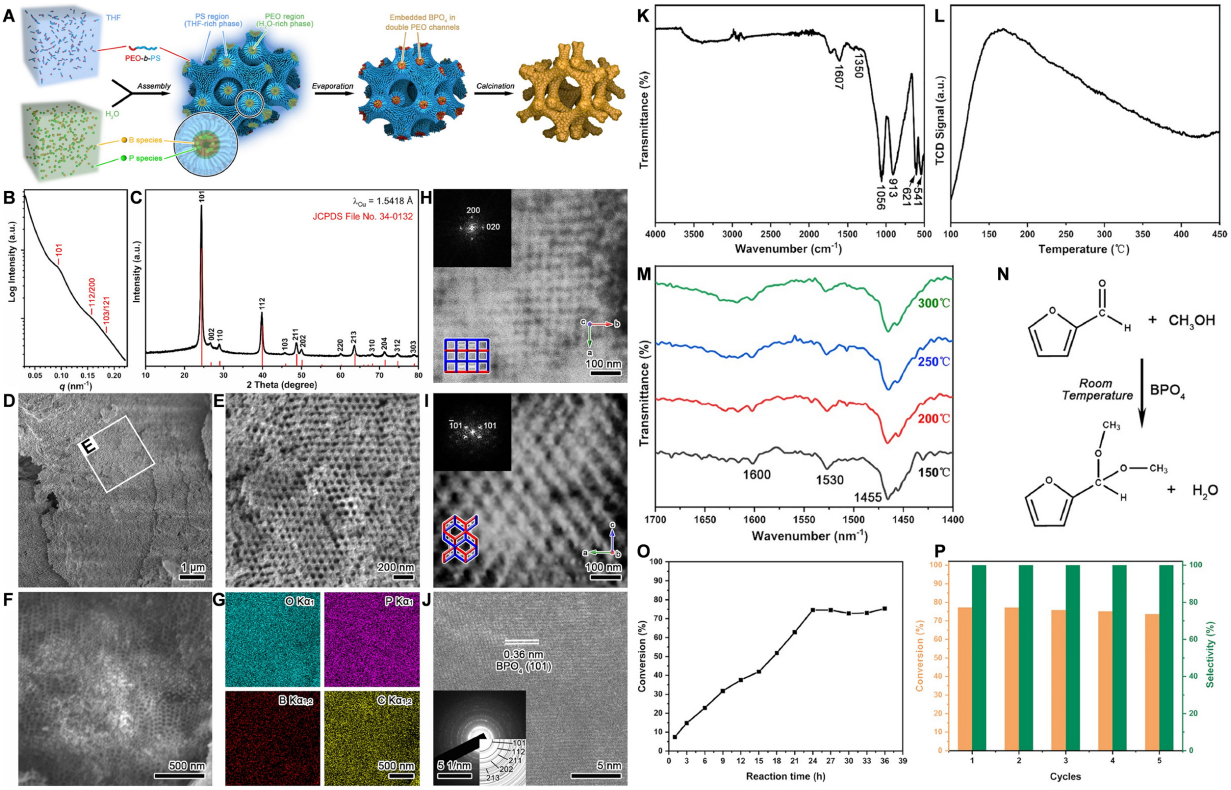


Figure 9. (A) Schematic drawing of the synthetic strategy of crystalline SDD BPO_4 scaffold; (B-M) Characterizations of crystalline SDD BPO_4 scaffold. (B) SAXS pattern. (C) Wide-angle XRD pattern. (D) Low-magnification SEM image. (E) High-magnification SEM image as shown in the white box in (D). (F and G) EDS mapping. (H and I) STEM images and the corresponding Fourier diffractograms of SDD BPO_4 scaffold taken from the [001] and [010] directions, respectively. (J) High-resolution TEM (HRTEM) image of SDD BPO_4 scaffold corresponding to the (101) plane of BPO_4. The inset shows the selected area electron diffraction with the polycrystalline ring pattern. (K) FTIR spectrum. (L) Temperature-programmed desorption of ammonia profile. (M) Pyridine-adsorption FTIR spectrum; (N) Catalytic acetalization of furfural and methanol to 2-(dimethoxymethyl)furan; (O) Effect of reaction time on the acetalization; (P) Reusability tests of SDD BPO_4 for the acetalization. This figure is reproduced with permission[218]. Copyright 2024, Science China Press. THF: Tetrahydrofuran; PEO-*b*-PS: poly(ethylene oxide)-*b*-polystyrene; PEO: poly(ethylene oxide); SDD: shifted double diamond; SAXS: small-angle X-ray scattering; XRD: X-ray diffraction; SEM: scanning electron microscopy; STEM: scanning transmission electron microscopy; FTIR: Fourier transform infrared; EDS: energy dispersive X-ray spectroscopy.

(HGC-Pt) catalysts exhibited an electrochemically active surface area 3.6 times that of solid carbon counterparts and a mass activity 2.7 times that of commercial Pt/C, owing to enhanced mass transport and reactant accessibility from the hollow structure[28].

Li *et al.* also introduced ordered bicontinuous mesostructures into covalent organic frameworks (COFs) and metal-organic frameworks (MOFs) using TPHS structures templated from block copolymer self-assembly[240]. Filling MOF precursors into DP-structured cubosome templates, followed by coordination and template removal, yielded SP-structured MOFs (SP-MOFs), including SP-ZIF-8, SP-ZIF-67 and SP-HKUST-1. When SP-ZIF-8 was used as a bioreactor, the trypsin loading reached 325 μg·mg^{-1}, achieving 37% sequence coverage and 45 matched peptides in digestion of bovine serum albumin (BSA) within 30 min - significantly outperforming free enzyme and conventional ZIF-8 - while maintaining high activity after 5 cycles[240]. The ordered bicontinuous structure also enhances light utilization through multiple reflections. Using SDD-structured silica as a hard template, Liu *et al.* synthesized SDD-COFs with hierarchical pore structures, overcoming the pore-blockage limitation of microporous or small-mesoporous COFs[239]. Benefiting from enhanced mass transport, improved light utilization and promoted photogenerated carrier separation, SDD-COFs performed excellently in visible-light-driven photocatalytic NO removal. A vinylene-linked COF (SDD-COF-3) achieved a NO conversion rate of 51.4%, far exceeding its non-mesoporous counterpart and

the classical photocatalyst g-C_3N_4, with excellent cycling stability. This provides a strategy for improving the accessibility of internal active sites in COFs and developing efficient photocatalysts[239].

The periodic channels of TPHSs enhance light harvesting through multiple reflections. The interconnected channels and frameworks reduce ion/electron charge-transfer resistance, markedly improving electrode reaction kinetics. The saddle-shaped non-positive-Gaussian-curvature surface lowers the free energy of catalytic intermediates (density functional theory), and enhances the interfacial electric field, promoting ion adsorption (finite element simulations). The highly symmetric periodic structure also alleviates charge-discharge mechanical stress, extending device cycle life[11,13,252]. Tang *et al.*[214,244], Xiang *et al.*[215], and Li *et al.*[253] explored electrochemical energy storage using DP-structured cubosomes from SEOs as templates, which have one set of open channels and another enclosed by the copolymer bilayer. Filling the open channels with various precursors and removing the template yields SP-structured bicontinuous mesoporous materials. An SP polypyrrole (SP-PPy) network served as the cathode host for Na-I_2 batteries: the bicontinuous structure facilitates iodine loading and electrolyte infiltration, and positively charged polaron/bipolaron groups adsorb polyiodide ions (I_3^-) through electrostatic interactions, suppressing the I_3^- shuttle effect. This cathode achieved a record-high specific capacity of 235 mA·h·g^{-1} at 0.5 C[215]. SP-PBA, a sodium-ion cathode from slow crystallization of Prussian blue analogs (PBAs) via HCl vapor diffusion, showed enhanced sodium-ion diffusion kinetics and uniform stress distribution during Na^+ intercalation, achieving 79.3% capacity retention after 3,000 charge-discharge cycles[214]. Polymerization of 3-aminophenol with formaldehyde within the open channels, followed by argon pyrolysis, produced SP-structured hard carbon (SP-HC) as a sodium-ion anode. Its saddle-shaped curvature increased carbon-framework defect density [observed by high-resolution TEM (HRTEM), Raman spectroscopy, X-ray diffraction (XRD), X-ray photoelectron spectroscopy and electron paramagnetic resonance; proposed based on these results], providing more Na^+ adsorption sites, while the expanded 4.0 Å interlayer spacing enabled nearly barrier-free Na^+ intercalation. SP-HC achieved a capacity of 172 mA·h·g^{-1} at 10 A·g^{-1} (full charge within 1 minute) and maintained a capacity of 80 mA·h·g^{-1} after 100,000 cycles, a record for hard-carbon sodium-ion anodes[244]. A marine-sponge-inspired carbonaceous sulfur host (bimeso-CoNC) featuring an SP structure and Co-N_4 single-atom sites was synthesized by filling the template with a Co-doped ZIF-8 precursor and pyrolyzing under argon. Its mesoporous channels (~ 31 nm) ensured rapid Li^+ transport and high sulfur loading, while the Co-N_4 single-atom sites suppressed the polysulfide shuttle effect and accelerated sulfur conversion. The bimeso-CoNC/S cathode maintained 570 mA·h·g^{-1} at 6 C and an areal capacity of 11.6 mA·h·cm^{-2} at 13.5 mg·cm^{-2}, with only 0.039% capacity decay per cycle over 1,200 cycles[253].

Werner *et al.* departed from conventional layered lithium-ion battery architectures by sequentially constructing three spatially continuous functional components separated by an electrolyte layer[254]. An oligomeric phenol-formaldehyde resol (the carbon precursor for the anode) was co-assembled with PI-*b*-PS-*b*-PEO into a core-shell DG structure. After inert calcination, a gyroidal carbon framework remained. Poly(phenylene oxide) (PPO) was electropolymerized onto the carbon as a solid-state electrolyte, and a sulfur/poly(3,4-ethylenedioxythiophene) (PEDOT) composite was infiltrated as the cathode, forming a complete lithium-ion battery whose areal capacity is theoretically 4,700 times that of a planar thin-film battery with the same critical dimensions[254]. Digital light processing (DLP) 3D printing was used to fabricate a monolithic G-structured solid oxide cell, eliminating the metallic interconnects and seals that typically account for over 75% of stack weight. Its specific power and volumetric power density exceeded 1 W·g^{-1} and 3 W·cm^{-3}, respectively (nearly an order of magnitude above planar stacks), with excellent stability during hundreds of hours of operation, reversible cycling, and thermal cycling - a new pathway for weight/volume-sensitive applications such as aerospace and portable power[255].

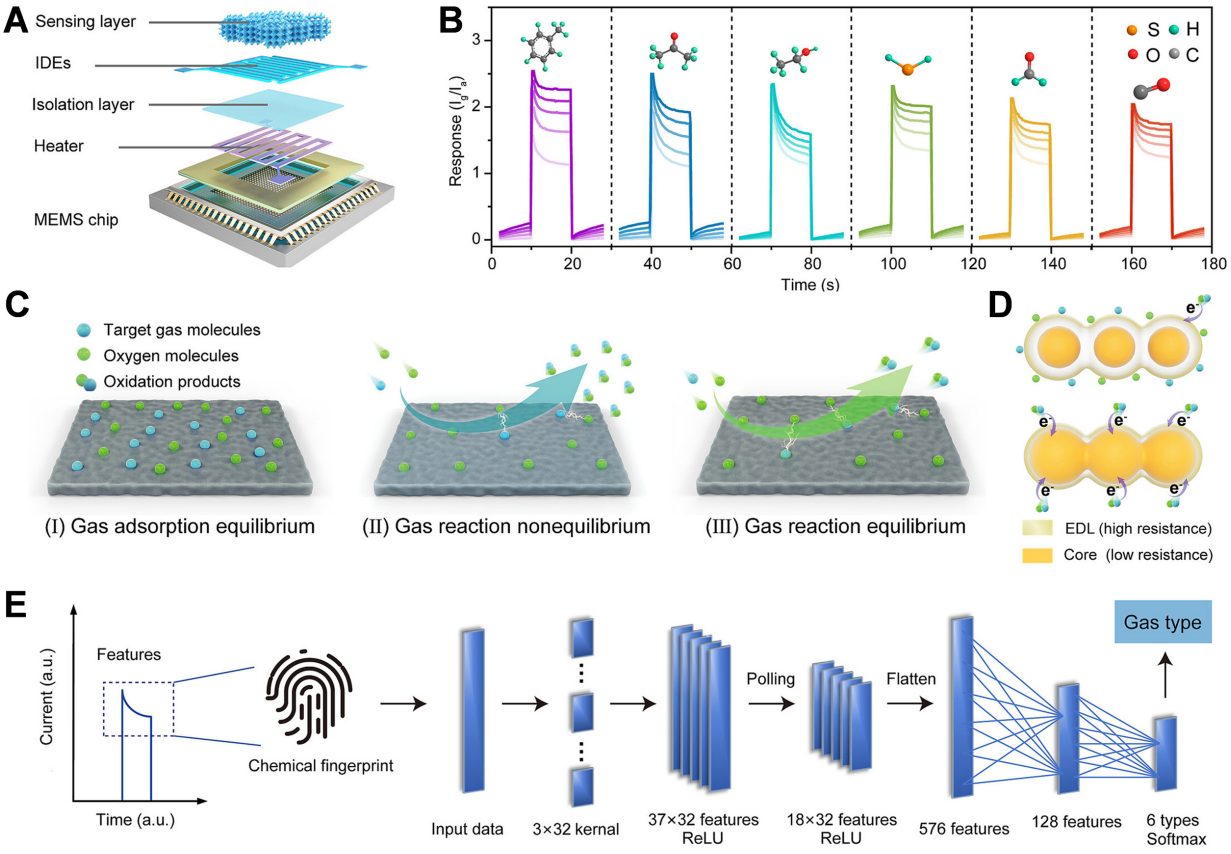


Figure 10. Gas sensor based on SP-structured SnO_2. (A) Schematic illustration of the sensor structure; (B) Single-cycle response curves of six representative gases under pulse heating; (C) Surface states of the metal oxide semiconductor during the gas sensing test; (D) Sensing mechanism toward gas molecules; (E) Extraction of overshoot peak data and gas recognition based on a convolutional neural network model. This figure is reproduced under the terms of the CC BY-NC-ND 4.0 License[7]. Copyright 2026, The Authors. IDE: interdigitated electrode; MEMS: microelectromechanical systems; EDL: electron depletion layer; SP: single primitive.

Owing to pore channels that enable rapid mass transport and full utilization of active sites, TPHS structures are also widely employed in sensors to enhance signal response[7,224-226,256]. Pang *et al.* utilized the P structure as the mechanical scaffold of a triboelectric nanogenerator (TENG), designing a linear thickness gradient that forms three layers of different wall thicknesses along the *z*-axis[225]. The P structure serves as the positive triboelectric layer and supporting scaffold, and its layer-by-layer compression deformation endows the device with three distinguishable electrical signal modes corresponding to long-distance, medium-distance and emergency braking states, so the braking condition can be identified in real time from the output voltage peak and duration - a novel sensing solution for autonomous-driving braking safety[225]. Inspired by the periodic porous membrane and breathing of the mammalian respiratory system, Chen *et al.* synthesized DP-structured cubosome templates from SEO, impregnated them with $SnCl_4 \cdot 5H_2O$ solution, and calcined the products to obtain SP-structured mesoporous SnO_2, which was deposited onto microelectromechanical systems (MEMS) chips as the sensing layer[7] [Figure 10A]. At low temperatures, gas is adsorbed onto the SnO_2 surface; upon rapid heating, the reaction rate increases sharply while gas diffusion lags, dropping the surface gas concentration to the reaction equilibrium concentration and determining the overshoot-peak amplitude. SnO_2 is an n-type semiconductor, and surface-adsorbed oxygen extracts electrons from the conduction band to form an electron depletion layer (high resistance). When reducing gases react with the adsorbed oxygen, electrons are released back to the conduction band, thinning the depletion layer and decreasing the resistance (increasing current). Different gases exhibit distinct current change magnitudes and rates due to differences in transferred-electron number and reaction activation energies [Figure 10B-D]. Pulse heating combined with a convolutional neural network identified six types of gases from the shapes of the overshoot peaks with 99.8% accuracy[7] [Figure 10E].

TPHS structures are advantageous for integrated compact heat exchange and catalytic reforming owing to their extremely high specific surface area, the boundary layer disruption effect of their complex internal channels and two mutually interconnected channels that can separately accommodate the heat-supplying and reacting fluids - making TPHSs an ideal platform combining compactness, efficiency and design flexibility in thermo-fluid-reaction multi-physics coupled systems[235,257-260]. Zhao *et al.* embedded the G structure into the cooling tube of a metal hydride hydrogen storage reactor to enhance heat dissipation[261]. Computational fluid dynamics simulations showed that the tortuous channels disturb the cooling fluid, inducing repeated flow impingement, flow-direction alterations and vortex formation, thereby generating turbulence without specialized processes. The solid-G reactor reduced the time to reach 1.2 wt.% hydrogen storage capacity by 23.40% and the peak average bed temperature rise by 9.49% relative to the conventional reactor[261]. Chen *et al.* compared serpentine channels with G, D and I-WP cold plates for electronic chip cooling[262]. The D structure performed best: under a heat flux of 140 $W \cdot cm^{-2}$, the maximum chip-surface temperature was reduced by 14.73 °C compared to the serpentine channel, owing to its larger heat transfer surface area and stronger secondary flows. They then designed a graded D structure with the unit cell size varying linearly along the height direction. Its equivalent convective heat transfer coefficient was 8.10%-10.30% higher than that of the uniform structure, with only a 3.81% higher pressure drop. With pumping power below 2 W, heat dissipation reached 256.9 $W \cdot cm^{-2}$, an overall improvement of 3.58%-6.24%[262].

Photonic and phononic applications

Materials with TPHS structures possess a 3D periodic distribution of the dielectric constant that enables a photonic bandgap analogous to the electronic bandgap in semiconductors, forbidding light propagation within specific frequency ranges - the core mechanism of photonic crystals[263-265]. Certain TPHS structures, such as SG and SD, can open CBGs or wide-angle photonic bandgaps when the dielectric contrast and fill fraction are appropriate. When intrinsically chiral (e.g., SG), the structure manipulates the polarization state of light, while dielectric contrast and fill fraction allow control of its dispersion. The bandgap position and width are tailored by adjusting structural parameters such as volume fraction, unit cell size, and network shift[1,266,267]. These properties are fundamentally enabled by the geometric topology of TPHSs, which dictates how electromagnetic waves are scattered, dispersed and polarized.

The SD structure has been called the "holy grail" of photonic crystals[26]. Bandgap calculations on shifted tG structures indicate that such distortions also provide an effective route to photonic bandgaps[208]. Cui *et al.* combined Fourier analysis with deep learning to explore photonic bandgaps across six space groups, confirming the superiority of SD and SG while discovering that the *lcs* topology with space group $Ia\bar{3}d$ approaches SD performance, warranting further investigation[29]. Flavell *et al.* simulated the programmed self-assembly of SG colloidal photonic crystals using two types of patchy spheres - both self-assembling into SG of either chiral enantiomer[238]. Bandgap calculations show that both the SG structures and their inverse structures support CBGs, requiring refractive index contrasts of approximately 2.7 and 2.2, respectively. Circular dichroism and transmission spectra verify their selective response to circularly polarized light, providing theoretical guidance for chiral photonic crystals and topological photonic devices[238]. Achieving visible bandgaps has long been challenging. Zhang *et al.* employed two-photon polymerization lithography and high-temperature annealing to fabricate SD titania photonic crystals with a patterning resolution reaching 180 nm and a refractive index of 2.4 to 2.6, whose reflectance within the photonic bandgap reaches ~ 100% in the visible range[268]. Jo *et al.* utilized high-molecular-weight (M_n = 680 kDa) polystyrene-*b*-poly(methyl methacrylate) (PS-*b*-PMMA) to prepare non-affinely distorted DG films with a lateral unit cell size of 335.7 nm via SVA, opening a visible-regime bandgap (center wavelength 562 nm)[269]. The optical chirality of SG originates from its intrinsic geometrical chirality and is more robust to local defects than that of negative-index metamaterials. Vignolini *et al.* fabricated SG gold metamaterial films with ~ 50 nm unit

cells: on twinned domains along the [110] projection, reflectance varied sinusoidally over 525-630 nm with rotating linear polarization (linear dichroism)[270]. Tilting by 35° and rotating around the [110] axis maximized the LH/RH circular-polarization transmission difference along the [111] chiral axis, experimentally verifying the optical chirality of SG[270]. The negative refraction of DG metallic metamaterials originates from the metal-insulator-metal (MIM) waveguide mode of their dual-network structure rather than geometrical chirality - supported by the mirror-symmetric SD also exhibiting a negative refraction band. This negative refraction band arises from band folding at the Brillouin zone boundary, with the refractive index continuously tunable by lattice size[271]. In topological photonics, DG and SG serve as ideal platforms for topological band degeneracies including Weyl points and line nodes. Lu *et al.* theoretically designed DG-based photonic crystals with broken parity and time-reversal symmetries, predicting frequency-isolated Weyl points whose topologically nontrivial surface states manifest as Fermi arcs connecting Weyl points of opposite chirality[272,273]. Weyl points in DG were experimentally verified at microwave frequencies through angle-resolved transmission measurements. Space group theory revealed that SG can open a bandgap between the second and third bands, whereas DG cannot, and that the glide-Z_2 topological invariant in DG is determined by the parity of the number of bands below the gap. Topological one-way fibers based on helical modulation of DG achieved one-way transmission protected by the second Chern number, creating new opportunities throughout photonics[272-279].

The generation and characteristics of phononic bandgaps depend on intrinsic material properties (including density and component volume fractions), and are significantly influenced by structural parameters such as symmetry, connectivity and geometric configuration[280-285]. Periodic minimal surfaces have recently been introduced into acoustic/elastic wave manipulation. Integrating acoustic metamaterial design with topological concepts provides a new pathway for lightweight and multifunctional acoustic devices[237,286]. Wu *et al.*[287] combined the micro-perforated plate (MPP) with a TPHS sandwich structure and investigated its sound transmission loss and absorption. Experiments and simulations demonstrate that MPPs provide significant sound-absorption capability within specific bands, while improving sound insulation through enhanced acoustic energy dissipation[287]. Further optimization of the G-type MPP-TPHS sandwich structure reveals that non-uniform perforation broadens the absorption bandwidth and improves overall acoustic performance, guiding the design of lightweight sandwich structures integrating load-bearing with sound insulation and absorption[287]. Among the 16 bicontinuous cubic network structures, the I-WP structure was identified as the champion phononic bandgap structure with the largest complete phononic bandgap (width 0.41) at its optimal volume fraction and strut thickness for a bismuth telluride network in an epoxy matrix, by finite difference frequency domain calculations[237]. Chen *et al.* designed and experimentally validated a 3D I-WP acoustic crystal, achieving a double-zero index, where the normalized effective mass density and effective compressibility simultaneously equal zero[286]. Exciting a four-fold degenerate cone formed by the degeneracy of one monopolar mode and three dipolar modes at the Dirac point frequency produces acoustic void behavior. Experiments confirmed that the acoustic crystal maintains a planar wavefront in a 90° bent waveguide and achieves acoustic cloaking when an internal obstacle is introduced[286].

Mechanical applications

TPHSs attract significant attention in mechanical metamaterials for their lightweight nature and outstanding mechanical properties. The non-positive-Gaussian-curvature regions distribute loads and reduce stress concentrations, enhancing load-bearing capacity (supported by both experimental and computational studies). Under impact or compression, their lattices undergo significant deformation, absorbing and dissipating substantial energy. Because sheet-based TPHS structures exhibit relatively homogeneous stress distributions, their fatigue performance generally exceeds that of conventional lattices at equivalent porosity and under well-controlled printing conditions, whereas printing defects and internal porosity can introduce local stress concentrations and degrade this advantage. Their geometry and mechanical properties can be

tailored by adjusting the parameters of their governing structural equations[288-295]. Zhang *et al.* systematically investigated the mechanical properties of 3D-printed TPHS structures, proposing a transition from finite regulation of known TPHSs to the infinite design capability of arbitrary TPHSs[30,241-243]. Inspired by crystal twinning, they introduced twin boundaries into G and D structures. Blocking stress transfer paths and introducing structural symmetry transformed the shear bands from wide and irregular distributions into symmetric ones, avoiding catastrophic failure at low strains in D[243]. In G structures, the chirality and number of SG networks significantly affect mechanical properties: racemic structures exhibited peak-stress improvements of up to 51.14% over homochiral structures, because the alternating LH/RH networks create alternating and opposing stress transfer paths, leading to more uniform stress distribution[241]. Eight bifurcating TPHS structures with non-cubic symmetry generally outperformed the classical G, D and P structures: tD-tDelta-L (loaded along the left side of tD-tDelta) showed a 26.5% improvement over D-[100] (loaded along the [100] direction of D), and tP-oPa-L (loaded along the left side of tP-oPa) showed a 41% improvement over P-[100] (loaded along the [100] direction of P). The bifurcating structures maintained minimal-surface characteristics under non-cubic deformation, exhibiting more flexible deformation adaptability[242]. They also proposed a free modeling method based on Fourier synthesis that constructs arbitrary periodic smooth surfaces by superimposing Fourier components corresponding to different Bragg reflections [Figure 11A and B], overcoming the limited scope of conventional level-set equations. It achieved an 86.21% increase in peak stress for a Fourier-designed P-derived structure (N-c_{111}-0.478) over the conventional P surface (N-c_{100}-fit) [Figure 11C-E] and a 98.02% improvement in energy absorption through optimized wall thickness distribution (P-position2) over the uniform P structure (P-uniform) [Figure 11F-K], and enabled non-equilibrium TPHS structures assembled via mortise-tenon joints[30]. These works establish a paradigm for TPHS mechanical metamaterials, transitioning from finite structures to infinite possibilities.

CONCLUSION AND OUTLOOK

This review covers TPHSs in biological systems, artificial self-assembly, and applications. In biological systems, the focus is on the analytical methods and formation mechanisms of TPHS structures in organisms such as butterflies and beetles. In artificial self-assembly, starting from liquid crystals and block copolymers, and following the trajectory from classical bicontinuous to single-network, symmetry-broken and high-genus topologies, this review summarizes the theoretical predictions and experimental advances in bottom-up fabrication of TPHS materials. In applications, functional advantages are summarized across multiple fields, centered on connectivity/topology, surface-area and pore-size and curvature-specific effects. Although significant progress has been made, several shortcomings remain.

(i) The structural diversity of artificial systems remains inferior to that of nature. SG and SD structures have been fabricated through self-assembly of block copolymers or liquid crystals and template methods. However, limitations remain, including limited structural tunability, relatively small unit cell parameters, and insufficient long-range order - leaving a considerable gap relative to natural counterparts. This disparity stems from our limited understanding of how organisms construct precise TPHS architectures across molecular, cellular and tissue scales. Specifically, the chiral selection of SG, the “smoothing” process in butterfly wing scales and the selective filling of I-WP subspaces by cells in beetles remain unresolved. Combining biology, 3D electron tomography and in vitro reconstruction models holds promise for revealing how nature achieves precise TPHS construction and for providing new self-assembly pathways. Stabilizing structures not yet achieved in artificial systems may require more sophisticated molecular design and modulation of packing frustration. Only by deeply understanding local curvature regulation, spatially selective filling, and kinetic pathway control can we provide design concepts that transcend existing paradigms.

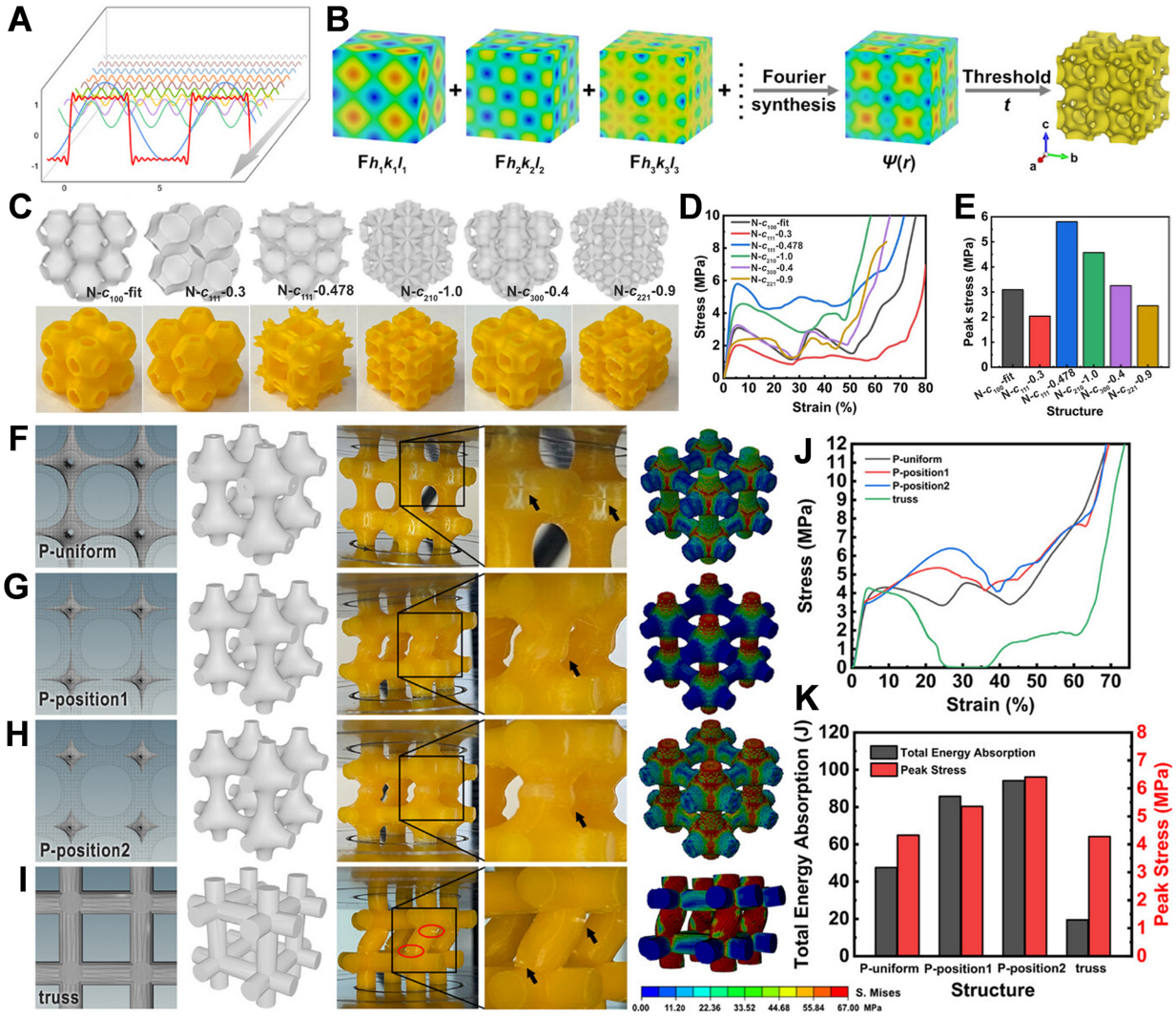


Figure 11. (A) Schematic drawing of the principle of Fourier synthesis; (B) Construction of TPHS structures; (C) Various structures were constructed based on $Pm\bar{3}m$ symmetry by adjusting corresponding Fourier components; (D) Stress-strain curves and (E) Peak stress of each structure in (C); (F-K) Structural mechanics optimization through the regulation of surface curvature and position based on Fourier synthesis; (F-I) show the models and deformation mechanisms of P structure with uniform wall thickness (F), optimized P structure with the nodes relatively thickened (G), optimized P structure with the struts relatively thickened (H) and the traditional truss structure (I); The solid and shaded parts represent the inner and outer walls of the structure, respectively. The black arrows in the enlarged images indicate where the deformation occurs; (J) Stress-strain curves of these structures; (K) Values of peak stress and total energy absorption extracted from the stress-strain curves. This figure is reproduced under the terms of the CC BY 4.0 License[30]. Copyright 2025, The Authors. TPHS: Triply periodic hyperbolic surface.

(ii) A deeper mechanistic understanding is essential for rational design of TPHS structures. In block copolymer self-assembly, limited theoretical predictive capability and intermediate-state characterization constitute critical bottlenecks. Most existing simulations struggle to address structural evolution under complex experimental conditions involving hydrolysis and condensation of inorganic precursors, multi-component cooperative assembly and kinetic pathway dependence. Moreover, predictions of metastable phases such as SG, SD and symmetry-broken structures often rely on specific molecular design assumptions and lack general theoretical guidance, making inverse design from target structures to synthesis parameters still unattainable. Although in situ characterization has advanced (e.g., cryo-electron microscopy, time-resolved SAXS), real-time capture of intermediate states remains constrained by spatiotemporal resolution and sample preparation difficulties, resulting in substantial loss of kinetic pathway information. This dual limitation prevents establishing a complete evolutionary pathway from initial conditions to final structures,

seriously hindering the upgrade of TPHS materials from empirical trial-and-error to rational design.

(iii) The chemical effects of non-positive Gaussian curvature remain largely unexplored. In physical applications, TPHS materials leverage their intrinsic geometric topological features, whereas in chemical applications such as catalysis and drug delivery, their advantages derive mainly from the high specific surface area, pore size, and three-dimensionally interconnected channels that provide superior mass transport. However, how the non-positive-Gaussian-curvature surface itself influences the microenvironment of chemical reactions, molecular adsorption and diffusion, the spatial distribution of active sites, and their performance remains insufficiently investigated. Future research should unravel the structure-activity relationship between the curvature geometry of TPHSs and chemical functionality, providing a new dimension for functional material design. In addition, most TPHS-based functional materials remain at the proof-of-concept stage; their long-term stability and compatibility with existing micro- and nanofabrication processes must be addressed to promote their practical application.

DECLARATIONS

Authors' contributions

Writing-original draft: Ye, S.
Writing-review & editing: Han, L.

Availability of data and materials

Not applicable.

AI and AI-assisted tools statement

During the preparation of this manuscript, the AI tool DeepSeek (version V4-Flash, released 2026-04-24) was used solely for language editing. The tool did not influence the study design, data collection, analysis, interpretation, or the scientific content of the work. All authors take full responsibility for the accuracy, integrity, and final content of the manuscript.

Financial support and sponsorship

This work was supported by the National Natural Science Foundation of China (No. 22425303) and the Fundamental Research Funds for the Central Universities.

Conflicts of interest

Han, L. is an Associate Editor of the journal *Micro Nano Science*. Han, L. was not involved in any steps of editorial processing, notably including reviewer selection, manuscript handling, and decision-making, while the other author has declared no conflicts of interest.

Ethical approval and consent to participate

Not applicable.

Consent for publication

Not applicable.

Copyright

© The Author(s) 2026.

REFERENCES

1. Han, L.; Che, S. An overview of materials with triply periodic minimal surfaces and related geometry: from biological structures to self-assembled systems. *Adv. Mater.* **2018**, *30*, e1705708. DOI PubMed
2. Emmer, M. Architecture and mathematics: soap bubbles and soap films. In: Williams K, Ostwald MJ, editors. Architecture and mathematics from antiquity to the future. Cham: Springer International Publishing; 2015. pp. 449-58. DOI
3. Schwarz, H. A. Gesammelte mathematische Abhandlungen; Springer Berlin, Heidelberg, 1890; Vol. 1. DOI

4. Neovius, E. R. Bestimmung zweier speciellen periodischen Minimalflächen, auf welchen unendlich viele gerade Linien und unendlich viele ebene geodätische Linien liegen; Frenckell: Helsingfors, 1883. (in German). https://resolver.sub.uni-goettingen.de/purl?PPN591417707.
5. Schoen, A. H. Infinite periodic minimal surfaces without self-intersections; NASA Technical Note NASA TN D-5541; National Aeronautics and Space Administration: Washington, D.C., 1970. https://ntrs.nasa.gov/citations/19700020472.
6. Xiang, L.; Li, Q.; Li, C.; Yang, Q.; Xu, F.; Mai, Y. Block copolymer self-assembly directed synthesis of porous materials with ordered bicontinuous structures and their potential applications. *Adv. Mater.* **2023**, *35*, e2207684. DOI
7. Chen, K.; Deng, Y.; Hu, T.; et al. Bioinspired periodic mesoporous tin oxides enable steady nonequilibrium chemical sensing for enhanced gas discrimination. *Proc. Natl. Acad. Sci. U. S. A.* **2026**, *123*, e2531153123. DOI PubMed PMC
8. Sheng, Q.; Li, Q.; Xiang, L.; Huang, T.; Mai, Y.; Han, L. Double diamond structured bicontinuous mesoporous titania templated by a block copolymer for anode material of lithium-ion battery. *Nano Res.* **2021**, *14*, 992-7. DOI
9. Mall, A. P.; Bhandarkar, V. V.; Mandaloi, G.; Tandon, P. An overview of design and development of biomimetic bone scaffolds using heterogeneous TPMS lattice structures. *Arch. Comput. Methods Eng.* **2025**, *32*, 2429-56. DOI
10. Liao, Y.; Liu, Y.; Ren, L.; et al. Nature-inspired bicontinuous-topology 3D-printed TPMS solar interfacial evaporator. *Chem. Eng. J.* **2026**, *536*, 176094. DOI
11. Xiang, L.; Tang, C.; Xu, Z.; Xu, F.; Li, C.; Mai, Y. Functional porous cubosomes: synthesis and applications in energy storage and conversion. *Acc. Mater. Res.* **2025**, *6*, 939-51. DOI
12. Sheng, Q.; Mao, W.; Han, L.; Che, S. Fabrication of photonic bandgap materials by shifting double frameworks. *Chemistry* **2018**, *24*, 17389-96. DOI PubMed
13. Li, C.; Li, Q.; Kaneti, Y. V.; Hou, D.; Yamauchi, Y.; Mai, Y. Self-assembly of block copolymers towards mesoporous materials for energy storage and conversion systems. *Chem. Soc. Rev.* **2020**, *49*, 4681-736. DOI
14. Cui, C.; Deng, Y.; Han, L. Bicontinuous cubic phases in biological and artificial self-assembled systems. *Sci. China Mater.* **2020**, *63*, 686-702. DOI PubMed PMC
15. Thayer, R. C.; Patel, N. H. A meta-analysis of butterfly structural colors: their color range, distribution and biological production. *J. Exp. Biol.* **2023**, *226*, jeb245940. DOI PubMed
16. Ban, M.; Kim, S.; Lee, J. Polymer cubosome-templated bicontinuous materials: design principles, synthesis, and energy-environmental applications. *Mater. Today* **2026**, *97*, 103338. DOI
17. Ranjith, M.; Khandke, S. A.; Niha, R.; Ansari, S.; Tamilnila, S. Bicontinuous cubic phase lipid nanoparticles cubosomes: formulation, characterization, and therapeutic applications. *J. Drug Deliv. Ther.* **2026**, *16*, 173-81. DOI
18. Bhatt, A. H.; Patel, H. P.; Patel, P. R.; et al. Cubosomes in non-oral drug delivery: advancing precision therapeutics from bench to bedside. *Int. J. Pharm.* **2025**, *684*, 126108. DOI
19. Barriga, H. M. G.; Holme, M. N.; Stevens, M. M. Cubosomes: the next generation of smart lipid nanoparticles? *Angew. Chem. Int. Ed. Engl.* **2019**, *58*, 2958-78. DOI PubMed PMC
20. Seidel, R.; Handrich, K.; Albéric, M.; et al. Comparative structural analysis of stereom polymorphs in the sea urchin test. *Faraday Discuss.* **2025**, *261*, 340-58. DOI
21. Yang, T.; Chen, H.; Jia, Z.; et al. A damage-tolerant, dual-scale, single-crystalline microlattice in the knobby starfish, *Protoreaster nodosus*. *Science* **2022**, *375*, 647-52. DOI
22. Zhao, X.; Xiong, Y.; Wang, W.; Zhang, W.; Zhang, D. Achieving structural white inspired by quasiordered microstructures in *Morpho theseus*. *NPG Asia Mater.* **2023**, *15*, 463. DOI
23. Kobayashi, Y.; Ohnuki, R.; Yoshioka, S. Discovery of I-WP minimal-surface-based photonic crystal in the scale of a longhorn beetle. *J. R. Soc. Interface* **2021**, *18*, 20210505. DOI PubMed PMC
24. Tang, Y.; Xue, Y. N.; Yang, S. G.; et al. Gyroid Labyrinth of supertwisted double helices in a liquid crystal polymer. *Angew. Chem. Int. Ed. Engl.* **2026**, *65*, e22314. DOI PubMed PMC
25. Chen, C.; Poppe, M.; Poppe, S.; Tschierske, C.; Liu, F. Liquid organic frameworks: a liquid crystalline 8-connected network with body-centered cubic symmetry. *Angew. Chem. Int. Ed. Engl.* **2020**, *59*, 20820-5. DOI PubMed PMC
26. Wang, C.; Cui, C.; Deng, Q.; et al. Construction of the single-diamond-structured titania scaffold-recreation of the holy grail photonic structure. *Proc. Natl. Acad. Sci. U. S. A.* **2024**, *121*, e2318072121. DOI PubMed PMC
27. Lee, H.; Kwon, S.; Min, J.; et al. Thermodynamically stable plumber's nightmare structures in block copolymers. *Science* **2024**, *383*, 70-6. DOI
28. Lee, G. H.; Choi, S.; Yang, H.; et al. Self-assembled hollow gyroids with bicontinuous mesostructures: a highly robust electrocatalyst fixation platform. *Adv. Mater.* **2025**, *37*, e2412525. DOI PubMed PMC
29. Cui, C.; Wei, G.; Saba, M.; Cao, Y.; Han, L. Deep learning-assisted Fourier analysis for high-efficiency structural design: a case study on three-dimensional photonic crystals enumeration. *Small* **2026**, *22*, e11158. DOI PubMed

30. Zhang, Y.; Zhang, J.; Zhou, Z.; et al. Multi-mechanical regulation of 3D printed triply periodic hyperbolic surfaces via fourier synthesis-based free modeling. *Adv. Sci. (Weinh).* **2025**, *12*, e70028. DOI PubMed PMC
31. Schamberger, B.; Ziege, R.; Anselme, K.; et al. Curvature in biological systems: its quantification, emergence, and implications across the Scales. *Adv. Mater.* **2023**, *35*, e2206110. DOI
32. Himmelmann, M.; Pedersen, M. C.; Klatt, M. A.; Schönhöfer, P. W. A.; Evans, M. E.; Schröder-Turk, G. E. Amorphous bicontinuous minimal surface models and the superior Gaussian curvature uniformity of diamond, primitive and gyroid surfaces. *P. Roy. Soc. A-Math. Phy.* **2026**, *482*, 20250275. DOI
33. Brakke, K. A. The surface evolver. *Exp. Math.* **1992**, *1*, 141-65. DOI
34. Huse, D. A.; Leibler, S. Phase behaviour of an ensemble of nonintersecting random fluid films. *J. Phys. France* **1988**, *49*, 605-21. DOI
35. Grosse-Brauckmann, K. Triply periodic minimal and constant mean curvature surfaces. *Interface Focus* **2012**, *2*, 582-8. DOI PubMed PMC
36. Grosse-Brauckmann, K. On gyroid interfaces. *J. Colloid Interface Sci.* **1997**, *187*, 418-28. DOI PubMed
37. Maldovan, M.; Urbas, A. M.; Yufa, N.; Carter, W. C.; Thomas, E. L. Photonic properties of bicontinuous cubic microphases. *Phys. Rev. B* **2002**, 65. DOI
38. Saba, M.; Wilts, B. D.; Hielscher, J.; Schröder-Turk, G. E. Absence of circular polarisation in reflections of butterfly wing scales with chiral gyroid structure. *Mater. Today: Proc.* **2014**, *1*, 193-208. DOI
39. Maldovan, M.; Thomas, E. L. Diamond-structured photonic crystals. *Nat. Mater.* **2004**, *3*, 593-600. DOI PubMed
40. Saranathan, V.; Osuji, C. O.; Mochrie, S. G.; et al. Structure, function, and self-assembly of single network gyroid ($I4_132$) photonic crystals in butterfly wing scales. *Proc. Natl. Acad. Sci. U. S. A.* **2010**, *107*, 11676-81. DOI PubMed PMC
41. Mao, W.; Cao, X.; Sheng, Q.; Han, L.; Che, S. Silica scaffold with shifted “plumber’s nightmare” networks and their interconversion into diamond networks. *Angew. Chem. Int. Ed. Engl.* **2017**, *56*, 10670-5. DOI PubMed
42. Li, H.; Liu, Y.; Cao, X.; Han, L.; Jiang, C.; Che, S. A shifted double-diamond titania scaffold. *Angew. Chem. Int. Ed. Engl.* **2017**, *56*, 806-11. DOI PubMed
43. Han, L.; Xu, D.; Liu, Y.; et al. Synthesis and characterization of macroporous photonic structure that consists of azimuthally shifted double-diamond silica frameworks. *Chem. Mater.* **2014**, *26*, 7020-8. DOI
44. Hsueh, H. Y.; Ho, R. M. Bicontinuous ceramics with high surface area from block copolymer templates. *Langmuir* **2012**, *28*, 8518-29. DOI PubMed
45. Andersson, S.; Hyde, S. T.; Larsson, K.; Lidin, S. Minimal surfaces and structures: from inorganic and metal crystals to cell membranes and biopolymers. *Chem. Rev.* **1988**, *88*, 221-42. DOI
46. Schröder-Turk, G. E.; Fogden, A.; Hyde, S. T. Bicontinuous geometries and molecular self-assembly: comparison of local curvature and global packing variations in genus-three cubic, tetragonal and rhombohedral surfaces. *Eur. Phys. J. B.* **2006**, *54*, 509-24. DOI
47. Anderson, D. M.; Davis, H. T.; Scriven, L. E.; Nitsche, J. C. C. Periodic surfaces of prescribed mean curvature. In: Prigogine I, Rice SA, editors. Advances in chemical physics. Wiley; 1990. pp. 337-96. DOI
48. Han, Y.; Zhang, D.; Chng, L. L.; et al. A tri-continuous mesoporous material with a silica pore wall following a hexagonal minimal surface. *Nat. Chem.* **2009**, *1*, 123-7. DOI
49. Hyde, S.; Schröder, G. Novel surfactant mesostructural topologies: between lamellae and columnar (hexagonal) forms. *Curr Opin Colloid In* **2003**, *8*, 5-14. DOI
50. Schwarz, U. S.; Gompper, G. Stability of bicontinuous cubic phases in ternary amphiphilic systems with spontaneous curvature. *J. Chem. Phys.* **2000**, *112*, 3792-802. DOI
51. Pappas, G. D.; Brandt, P. W. Mitochondria. I. fine structure of the complex patterns in the mitochondria of *Pelomyxa carolinensis* Wilson (*Chaos chaos* L.). *J. Biophys. Cytol.* **1959**, *6*, 85-90. DOI PubMed PMC
52. Borysko, E.; Roslansky, J. Methods for correlated optical and electron microscopic studies of amoebae*. *Ann. N. Y. Acad. Sci.* **1959**, *78*, 432-47. DOI
53. Daniels, E. W.; Breyer, E. P. Starvation effects on the ultrastructure of amoeba mitochondria. *Z. Zellforsch. Mikrosk. Anat.* **1968**, *91*, 159-69. DOI PubMed
54. Deng, Y.; Marko, M.; Buttle, K. F.; Leith, A.; Mieczkowski, M.; Mannella, C. A. Cubic membrane structure in amoeba (*Chaos carolinensis*) mitochondria determined by electron microscopic tomography. *J. Struct. Biol.* **1999**, *127*, 231-9. DOI PubMed
55. Deng, Y.; Mieczkowski, M. Three-dimensional periodic cubic membrane structure in the mitochondria of amoebae *Chaos carolinensis*. *Protoplasma* **1998**, *203*, 16-25. DOI
56. Almsherqi, Z.; Margadant, F.; Deng, Y. A look through ‘lens’ cubic mitochondria. *Interface Focus* **2012**, *2*, 539-45. DOI PubMed PMC
57. Bykowski, M.; Mazur, R.; Buszewicz, D.; Szach, J.; Mostowska, A.; Kowalewska, Ł. Spatial nano-morphology of the prolamellar body in etiolated *Arabidopsis thaliana* plants with disturbed pigment and polyprenol composition. *Front. Cell Dev. Biol.* **2020**, *8*, 586628. DOI PubMed PMC

58. Hain, T. M.; Bykowski, M.; Saba, M.; Evans, M. E.; Schröder-Turk, G. E.; Kowalewska, Ł. SPIRE-a software tool for bicontinuous phase recognition: application for plastid cubic membranes. *Plant Physiol.* **2022**, *188*, 81-96. DOI PubMed PMC
59. Michielsen, K.; De Raedt, H.; Stavenga, D. G. Reflectivity of the gyroid biophotonic crystals in the ventral wing scales of the Green Hairstreak butterfly, *Callophrys rubi*. *J. R. Soc. Interface* **2010**, *7*, 765-71. DOI PubMed PMC
60. Michielsen, K.; Stavenga, D. G. Gyroid cuticular structures in butterfly wing scales: biological photonic crystals. *J. R. Soc. Interface* **2008**, *5*, 85-94. DOI PubMed PMC
61. Argyros, A.; Manos, S.; Large, M. C.; McKenzie, D. R.; Cox, G. C.; Dwarte, D. M. Electron tomography and computer visualisation of a three-dimensional 'photonic' crystal in a butterfly wing-scale. *Micron* **2002**, *33*, 483-7. DOI
62. Prum, R. O.; Quinn, T.; Torres, R. H. Anatomically diverse butterfly scales all produce structural colours by coherent scattering. *J. Exp. Biol.* **2006**, *209*, 748-65. DOI PubMed
63. Schröder-Turk, G. E.; Wickham, S.; Averdunk, H.; et al. The chiral structure of porous chitin within the wing-scales of *Callophrys rubi*. *J. Struct. Biol.* **2011**, *174*, 290-5. DOI
64. Winter, B.; Butz, B.; Dieker, C.; Schröder-Turk, G. E.; Mecke, K.; Spiecker, E. Coexistence of both gyroid chiralities in individual butterfly wing scales of *Callophrys rubi*. *Proc. Natl. Acad. Sci. U. S. A.* **2015**, *112*, 12911-6. DOI PubMed PMC
65. Inoue, M.; Saito, K.; Aoyama, H.; Inoue, H.; Ohnuki, R.; Yoshioka, S. Study on the chirality of gyroid photonic crystals in butterfly wing scales. *Sci. Rep.* **2025**, *15*, 20968. DOI PubMed PMC
66. Wilts, B. D.; Apeleo Zubiri, B.; Klatt, M. A.; et al. Butterfly gyroid nanostructures as a time-frozen glimpse of intracellular membrane development. *Sci. Adv.* **2017**, *3*, e1603119. DOI PubMed PMC
67. Jessop, A. L.; Clode, P. L.; Saunders, M.; et al. Hierarchical woven fibrillar structures in developing single gyroids in butterflies. *Proc. Natl. Acad. Sci. U. S. A.* **2025**, *122*, e2507297122. DOI PubMed PMC
68. Corkery, R. W.; Tyrode, E. C. On the colour of wing scales in butterflies: iridescence and preferred orientation of single gyroid photonic crystals. *Interface Focus* **2017**, *7*, 20160154. DOI PubMed PMC
69. Jessop, A. L.; Pirih, P.; Wang, L.; et al. Elucidating nanostructural organization and photonic properties of butterfly wing scales using hyperspectral microscopy. *J. R. Soc. Interface* **2024**, *21*, 20240185. DOI PubMed PMC
70. Galusha, J. W.; Richey, L. R.; Gardner, J. S.; Cha, J. N.; Bartl, M. H. Discovery of a diamond-based photonic crystal structure in beetle scales. *Phys. Rev. E Stat. Nonlin. Soft Matter Phys.* **2008**, *77*, 050904. DOI PubMed
71. Wilts, B. D.; Michielsen, K.; Kuipers, J.; De, Raedt. H.; Stavenga, D. G. Brilliant camouflage: photonic crystals in the diamond weevil, *Entimus imperialis*. *Proc. Biol. Sci.* **2012**, *279*, 2524-30. DOI PubMed PMC
72. Wu, X.; Erbe, A.; Raabe, D.; Fabritius, H. Extreme optical properties tuned through phase substitution in a structurally optimized biological photonic polycrystal. *Adv. Funct. Mater.* **2013**, *23*, 3615-20. DOI
73. Saranathan, V.; Seago, A. E.; Sandy, A.; et al. Structural diversity of arthropod biophotonic nanostructures spans amphiphilic phase-space. *Nano Lett.* **2015**, *15*, 3735-42. DOI
74. Parisotto, A.; Steiner, U.; Cabras, A. A.; Van Dam, M. H.; Wilts, B. D. Pachyrhynchus weevils use 3D photonic crystals with varying degrees of order to create diverse and brilliant displays. *Small* **2022**, *18*, e2200592. DOI PubMed
75. Edagawa, K.; Kanoko, S.; Notomi, M. Photonic amorphous diamond structure with a 3D photonic band gap. *Phys. Rev. Lett.* **2008**, *100*, 013901. DOI PubMed
76. Djeghdi, K.; Steiner, U.; Wilts, B. D. 3D Tomographic analysis of the order-disorder interplay in the *Pachyrhynchus congestus mirabilis* weevil. *Adv. Sci. (Weinh).* **2022**, *9*, e2202145. DOI PubMed PMC
77. Bauernfeind, V.; Saranathan, V.; Djeghdi, K.; et al. Not only a matter of disorder in I-WP minimal surface-based photonic networks: diffusive structural color in *Sternotomis amabilis* longhorn beetles. *Mater. Today Adv.* **2024**, *23*, 100524. DOI
78. Bauernfeind, V.; Djeghdi, K.; Gunkel, I.; Steiner, U.; Wilts, B. D. Photonic amorphous I-WP-like networks create angle-independent colors in *Sternotomis virescens* Longhorn beetles. *Adv. Funct. Mater.* **2024**, *34*, 2302720. DOI
79. Saranathan, V.; Narayanan, S.; Sandy, A.; Dufresne, E. R.; Prum, R. O. Evolution of single gyroid photonic crystals in bird feathers. *Proc. Natl. Acad. Sci. U. S. A.* **2021**, *118*, e2101357118. DOI PubMed PMC
80. Donnay, G.; Pawson, D. L. X-ray diffraction studies of echinoderm plates. *Science* **1969**, *166*, 1147-50. DOI PubMed
81. Hyde, S. T.; Meldrum, F. C. Starfish grow extraordinary crystals. *Science* **2022**, *375*, 615-6. DOI PubMed
82. Jessop, A. L.; Millsteed, A. J.; Kirkensgaard, J. J. K.; Shaw, J.; Clode, P. L.; Schröder-Turk, G. E. Composite material in the sea urchin *Cidaris rugosa*: ordered and disordered micrometre-scale bicontinuous geometries. *J. R. Soc. Interface* **2024**, *21*, 20230597. DOI PubMed PMC
83. Nissen, H. U. Crystal orientation and plate structure in echinoid skeletal units. *Science* **1969**, *166*, 1150-2. DOI PubMed
84. Gorzelak, P.; Kołbuk, D.; Stolarski, J.; et al. A Devonian crinoid with a diamond microlattice. *Proc. Biol. Sci.* **2023**, *290*, 20230092. DOI PubMed PMC

85. Guo, X.; Li, X.; Wang, E.; Fuh, J. Y.; Lu, W. F.; Zhai, W. Bioinspired hierarchical diamond triply periodic minimal surface lattices with high energy absorption and damage tolerance. *Addit. Manuf.* **2023**, *76*, 103792. DOI
86. Wang, H. F.; Chiu, P. T.; Yang, C. Y.; et al. Networks with controlled chirality via self-assembly of chiral triblock terpolymers. *Sci. Adv.* **2020**, *6*, eabc3644. DOI PubMed PMC
87. Yang, K. C.; Reddy, A.; Tsai, H. W.; Zhao, W.; Grason, G. M.; Ho, R. M. Breaking mirror symmetry of double gyroids via self-assembly of chiral block copolymers. *ACS Macro Lett.* **2022**, *11*, 930-4. DOI PubMed
88. Hou, L.; Xu, Z.; Dong, Q.; Shi, A.; Li, W. Stabilizing DG, DD, and DP Bicontinuous network phases in pure AB-type block copolymers beyond relieving packing frustration. *Macromolecules* **2024**, *57*, 2165-75. DOI
89. Xie, Q.; Qiang, Y.; Li, W. Single gyroid self-assembled by linear BABAB pentablock copolymer. *ACS Macro Lett.* **2022**, *11*, 205-9. DOI
90. Cheng, Y.; Xu, Z.; Li, W. Understand the relative stability of single-gyroid to double-gyroid in AB-type block copolymer: chain packing and geometric analysis. *Macromolecules* **2024**, *57*, 9167-80. DOI
91. La, Y.; Park, C.; Shin, T. J.; Joo, S. H.; Kang, S.; Kim, K. T. Colloidal inverse bicontinuous cubic membranes of block copolymers with tunable surface functional groups. *Nat. Chem.* **2014**, *6*, 534-41. DOI
92. Ha, S.; La, Y.; Kim, K. T. Polymer cubosomes: infinite cubic mazes and possibilities. *Acc. Chem. Res.* **2020**, *53*, 620-31. DOI
93. Park, S. J.; Bates, F. S.; Dorfman, K. D. Single gyroid in H-shaped block copolymers. *Phys. Rev. Mater.* **2023**, 7. DOI
94. Cho, A.; La, Y.; Jeoung, S.; et al. Mix-and-match assembly of block copolymer blends in solution. *Macromolecules* **2017**, *50*, 3234-43. DOI
95. Chu, C.; Pei, R.; Chen, H. Order-order transition from ordered bicontinuous double diamond to hexagonally packed cylinders in stereoregular diblock copolymer/homopolymer blends. *Macromolecules* **2018**, *51*, 8493-500. DOI
96. Takagi, H.; Yamamoto, K.; Okamoto, S. Ordered-bicontinuous-double-diamond structure in block copolymer/homopolymer blends. *EPL* **2015**, *110*, 48003. DOI
97. Takagi, W.; Suzuki, J.; Aoyama, Y.; Mihira, T.; Takano, A.; Matsushita, Y. Bicontinuous double-diamond structures formed in ternary blends of ab diblock copolymers with block chains of different lengths. *Macromolecules* **2019**, *52*, 6633-40. DOI
98. Takagi, H.; Yamamoto, K. Effect of block copolymer composition and homopolymer molecular weight on ordered bicontinuous double-diamond structures in binary blends of polystyrene-polyisoprene block copolymer and polyisoprene homopolymer. *Macromolecules* **2021**, *54*, 5136-43. DOI
99. Wang, X.; Feng, Y.; Lu, S.; Feng, X.; Wang, G.; Li, W. SCFT-guided experimental fabrication of double-diamond structures in A_1B/A_2B block copolymer binary blends. *Macromolecules* **2025**, *58*, 9776-85. DOI
100. Duan, C.; Wang, Z. G. End-functionalized ions promote stability of highly frustrated phases in diblock copolymers. *Proc. Natl. Acad. Sci. U. S. A.* **2026**, *123*, e2621115123. DOI PubMed PMC
101. Hendeniya, N.; Chittick, C.; Hillery, K.; Abtahi, S.; Mosher, C.; Chang, B. Revealing the kinetic phase behavior of block copolymer complexes using solvent vapor absorption-desorption isotherms. *ACS Appl. Mater. Interfaces* **2024**, *16*, 18144-53. DOI PubMed PMC
102. Lin, Z.; Liu, S.; Mao, W.; et al. Tunable self-assembly of diblock copolymers into colloidal particles with triply periodic minimal surfaces. *Angew. Chem. Int. Ed. Engl.* **2017**, *56*, 7135-40. DOI
103. Dolan, J. A.; Korzeb, K.; Dehmel, R.; et al. Controlling self-assembly in gyroid terpolymer films by solvent vapor annealing. *Small* **2018**, *14*, e1802401. DOI
104. Chang, C.; Chen, Y.; Ho, R. Metastable network phases from controlled self-assembly of high- χ block copolymers. *Phys. Rev. Mater.* **2024**, *8*, 030301. DOI
105. Yeh, S. L.; Chang, C. Y.; Ho, R. M. Reticulation of block copolymer nanostructures from perforation. *ACS Appl. Mater. Interfaces* **2025**, *17*, 12676-85. DOI PubMed PMC
106. Jacobs, A. G.; Liedel, C.; Peng, H.; et al. Kinetics of block copolymer phase segregation during sub-millisecond transient thermal annealing. *Macromolecules* **2016**, *49*, 6462-70. DOI
107. Luan, J.; Wang, D.; Kok, N. P.; Moslehi, N.; Voets, I. K.; Wilson, D. A. Dynamic pathways in energy landscapes guiding supramolecular Janus dendrimer self-assemblies between lamellar and cubic architectures. *Nat. Commun.* **2025**, *16*, 8075. DOI PubMed PMC
108. Deng, Q.; Liu, Y.; Cao, Y.; Han, L. Formation of a silica scaffold with a hyperbolic surface structure as a time-frozen glimpse by ultraviolet curing. *Interface Focus* **2026**, *16*, 20250091. DOI
109. Feng, J.; Fu, J.; Yao, X.; He, Y. Triply periodic minimal surface (TPMS) porous structures: from multi-scale design, precise additive manufacturing to multidisciplinary applications. *Int. J. Extrem. Manuf.* **2022**, *4*, 022001. DOI
110. Koroľ, M.; Töröková, M.; Tkáč, J. Triply periodic minimal surface (TPMS) cellular structures: modeling, manufacturing, and application perspectives - a review. *J. Compos. Sci.* **2026**, *10*, 439. DOI

111. Lee, H.; Lee, D. H.; Hyun, J.; et al. Development and prospects of zirconia 3D printing for artificial prosthesis applications. *Chem. Rev.* **2026**, *126*, 8203-33. DOI
112. Pflaum, M.; Barbian, K. P.; Neuhaus, F.; et al. From fiber bundles to architected membranes: triply periodic minimal surface architectures for biohybrid artificial lungs. *Adv. Mater.* **2026**, *38*, e74361. DOI PubMed PMC
113. Wang, Y.; Lei, Y.; Cui, R.; et al. A genus-tuning design on minimal surfaces for open-cell mechanical metamaterials. *Int. J. Mech. Sci.* **2026**, *313*, 111304. DOI
114. Nuhu, A. A.; Elmoghazy, Y. H.; Al Mahmoud, Z.; Petrů, J.; Sahmani, S.; Safaei, B. TPMS-based hyperboloidal primitive architectured structures with a novel hybridization method. *Int. J. Mech. Sci.* **2026**, *312*, 111206. DOI
115. Daynes, S. Isotropic cellular structure design strategies based on triply periodic minimal surfaces. *Addit. Manuf.* **2024**, *81*, 104010. DOI
116. Fu, J.; Ding, J.; Zhang, L.; Qu, S.; Song, X.; Fu, M. Development of conformal shell lattices via laser powder bed fusion and unraveling their mechanical responses via modeling and experiments. *Addit. Manuf.* **2023**, *62*, 103406. DOI
117. Jin, Y.; Zou, S.; Pan, B.; Li, G.; Shao, L.; Du, J. Biomechanical properties of cylindrical and twisted triply periodic minimal surface scaffolds fabricated by laser powder bed fusion. *Addit. Manuf.* **2022**, *56*, 102899. DOI
118. Perna, I.; Ferraro, R.; Coppola, S.; Caserta, S. Phase separation in block copolymer systems: From thermodynamics to industrial applications. *Adv. Colloid Interface Sci.* **2026**, *352*, 103841. DOI PubMed
119. Hümöller, J. M.; Oviedo, O. A. Exploring liquid crystal properties through the two-phase thermodynamic model: structural, dynamic, and thermodynamic properties. *J. Chem. Theory Comput.* **2025**, *21*, 2219-34. DOI PubMed
120. Meng, Z.; Wang, S.; Xu, G.; Qiu, S.; Xu, X. Recent advances: kinetically controlled chiral matters for soft assembly, motion and optoelectronics. *Laser Photonics Rev.* **2025**, *19*, 2401754. DOI
121. Fielden, S. D. P. Kinetically controlled and nonequilibrium assembly of block copolymers in solution. *J. Am. Chem. Soc.* **2024**, *146*, 18781-96. DOI PubMed PMC
122. Xu, Z.; Dong, Q.; Li, W. Architectural design of block copolymers. *Macromolecules* **2024**, *57*, 1869-84. DOI
123. Chen, P.; Mahanthappa, M. K.; Dorfman, K. D. Stability of cubic single network phases in diblock copolymer melts. *J. Polym. Sci.* **2022**, *60*, 2543-52. DOI
124. Dimitriyev, M. S.; Reddy, A.; Grason, G. M. Medial packing, frustration, and competing network phases in strongly segregated block copolymers. *Macromolecules* **2023**, *56*, 7184-202. DOI
125. Dimitriyev, M. S.; Greenvall, B. R.; Mathew, R.; Grason, G. M. Not even metastable: cubic double-diamond in diblock copolymer melts. *ACS Macro Lett.* **2025**, *14*, 1291-8. DOI PubMed
126. Wang, L.; Urbas, A. M.; Li, Q. Nature-inspired emerging chiral liquid crystal nanostructures: from molecular self-assembly to DNA mesophase and nanocolloids. *Adv. Mater.* **2020**, *32*, e1801335. DOI PubMed
127. Bisoyi, H. K.; Li, Q. Light-directing chiral liquid crystal nanostructures: from 1D to 3D. *Acc. Chem. Res.* **2014**, *47*, 3184-95. DOI PubMed
128. Wang, Y.; Singh, G.; Agra-Kooijman, D. M.; et al. Room temperature heliconical twist-bend nematic liquid crystal. *CrystEngComm* **2015**, *17*, 2778-82. DOI
129. Ma, L. L.; Li, C. Y.; Pan, J. T.; et al. Self-assembled liquid crystal architectures for soft matter photonics. *Light Sci. Appl.* **2022**, *11*, 270. DOI PubMed PMC
130. Prakash, J.; Chandran, A.; Biradar, A. M. Scientific developments of liquid crystal-based optical memory: a review. *Rep. Prog. Phys.* **2017**, *80*, 016601. DOI PubMed
131. Govindan, I.; Paul, A.; Rama, A.; et al. Mesogenic architectures for advanced drug delivery: interrogating lyotropic and thermotropic liquid crystals. *AAPS PharmSciTech.* **2024**, *26*, 6. DOI
132. Shan, X.; Luo, L.; Yu, Z.; You, J. Recent advances in versatile inverse lyotropic liquid crystals. *J. Control. Release* **2022**, *348*, 1-21. DOI
133. Zhai, J.; Sarkar, S.; Tran, N.; Pandiancherri, S.; Greaves, T. L.; Drummond, C. J. Tuning nanostructured lyotropic liquid crystalline mesophases in lipid nanoparticles with protic ionic liquids. *J. Phys. Chem. Lett.* **2021**, *12*, 399-404. DOI PubMed
134. Mezzenga, R.; Seddon, J. M.; Drummond, C. J.; Boyd, B. J.; Schröder-Turk, G. E.; Sagalowicz, L. Nature-inspired design and application of lipidic lyotropic liquid crystals. *Adv. Mater.* **2019**, *31*, e1900818. DOI PubMed
135. Liang, B.; Cheng, Y.; Liu, X.; et al. Chiral liquid crystals based on pillararene and supramolecular self-assembly-induced chirality amplification. *Sci. China Chem.* **2024**, *67*, 3373-81. DOI
136. Shimomura, Y.; Tokita, M.; Kawamura, A.; Watanabe, J.; Konishi, G. Fluorinated poly(pentylene 4,4′-bibenzoate)s with low isotropization temperatures and unique phase transition behavior. *Macromolecules* **2023**, *56*, 5152-61. DOI
137. Che, A.; Zellmann-Parrotta, C. O.; Sarkar, D.; et al. Cyclodextrin-based liquid crystals: a novel approach to promote the formation of thermotropic cubic mesophases and their potential applications as electrolytes. *Carbohydr. Polym.* **2025**, *359*, 123587. DOI
138. Cao, Y.; Tschierske, C.; Liu, F. Structural complexity, network formation and spontaneous chirality in soft-matter self-assembly. *Acc. Chem. Res.* **2026**, *59*, 1983-96. DOI PubMed PMC

139. Levelut, A.; Clerc, M. Structural investigations on ‘smectic D’ and related mesophases. *Liq. Cryst.* **1998**, *24*, 105-16. DOI
140. Zeng, X.; Ungar, G.; Impéror-Clerc, M. A triple-network tricontinuous cubic liquid crystal. *Nat. Mater.* **2005**, *4*, 562-7. DOI PubMed
141. Zeng, X.; Prehm, M.; Ungar, G.; Tschierske, C.; Liu, F. Formation of a double diamond cubic phase by thermotropic liquid crystalline self-assembly of bundled bolaamphiphiles. *Angew. Chem. Int. Ed. Engl.* **2016**, *55*, 8324-7. DOI PubMed PMC
142. Zeng, X.; Poppe, S.; Lehmann, A.; et al. A self-assembled bicontinuous cubic phase with a single-diamond network. *Angew. Chem. Int. Ed. Engl.* **2019**, *58*, 7375-9. DOI
143. Poppe, S.; Cheng, X.; Chen, C.; et al. Liquid organic frameworks: the single-network “plumber’s nightmare” bicontinuous cubic liquid crystal. *J. Am. Chem. Soc.* **2020**, *142*, 3296-300. DOI
144. Cao, Y.; Alaasar, M.; Zhang, L.; Zhu, C.; Tschierske, C.; Liu, F. Supramolecular meso-trick: ambidextrous mirror symmetry breaking in a liquid crystalline network with tetragonal symmetry. *J. Am. Chem. Soc.* **2022**, *144*, 6936-45. DOI
145. Cai, X.; Hauche, S.; Poppe, S.; et al. Network phases with multiple-junction geometries at the gyroid-diamond transition. *J. Am. Chem. Soc.* **2023**, *145*, 1000-10. DOI
146. Cao, Y.; Alaasar, M.; Nallapaneni, A.; et al. Molecular packing in double gyroid cubic phases revealed via resonant soft X-ray scattering. *Phys. Rev. Lett.* **2020**, *125*, 027801. DOI
147. Poppe, S.; Chen, C.; Wagner, M.; Cao, Y.; Liu, F.; Tschierske, C. A series of three liquid crystalline cubic phases with an alternating sequence of single- and double-network structures. *Chem. Commun. (Camb)* **2025**, *61*, 18629-32. DOI PubMed
148. Luzzati, V.; Spegt, P. A. Polymorphism of lipids. *Nature* **1967**, *215*, 701-4. DOI
149. Luzzati, V.; Tardieu, A.; Gulik-Krzywicki, T. Polymorphism of lipids. *Nature* **1968**, *217*, 1028-30. DOI PubMed
150. Templer, R. H.; Seddon, J. M.; Warrender, N. A.; et al. Inverse bicontinuous cubic phases in 2:1 fatty acid/phosphatidylcholine mixtures. The effects of chain length, hydration, and temperature. *J. Phys. Chem. B.* **1998**, *102*, 7251-61. DOI
151. Tang, T. Y.; Seddon, A. M.; Jeworrek, C.; et al. The effects of pressure and temperature on the energetics and pivotal surface in a monoacylglycerol/water gyroid inverse bicontinuous cubic phase. *Soft Matter* **2014**, *10*, 3009-15. DOI
152. Vacklin, H.; Khoo, B. J.; Madan, K. H.; Seddon, J. M.; Templer, R. H. The bending elasticity of 1-monoolein upon relief of packing stress. *Langmuir* **2000**, *16*, 4741-8. DOI
153. Tang, T. Y.; Brooks, N. J.; Jeworrek, C.; et al. Hydrostatic pressure effects on the lamellar to gyroid cubic phase transition of monolinolein at limited hydration. *Langmuir* **2012**, *28*, 13018-24. DOI
154. Shearman, G. C.; Khoo, B. J.; Motherwell, M. L.; et al. Calculations of and evidence for chain packing stress in inverse lyotropic bicontinuous cubic phases. *Langmuir* **2007**, *23*, 7276-85. DOI
155. Tyler, A. I.; Barriga, H. M.; Parsons, E. S.; et al. Electrostatic swelling of bicontinuous cubic lipid phases. *Soft Matter* **2015**, *11*, 3279-86. DOI
156. Barriga, H. M.; Tyler, A. I.; McCarthy, N. L.; et al. Temperature and pressure tuneable swollen bicontinuous cubic phases approaching nature’s length scales. *Soft Matter* **2015**, *11*, 600-7. DOI
157. Kulkarni, C. V.; Tang, T.; Seddon, A. M.; Seddon, J. M.; Ces, O.; Templer, R. H. Engineering bicontinuous cubic structures at the nanoscale - the role of chain splay. *Soft Matter* **2010**, *6*, 3191. DOI
158. Tang, T. Y.; Brooks, N. J.; Ces, O.; Seddon, J. M.; Templer, R. H. Structural studies of the lamellar to bicontinuous gyroid cubic (Q_{II}^{G}) phase transitions under limited hydration conditions. *Soft Matter* **2015**, *11*, 1991-7. DOI PubMed
159. Tran, N.; Zhai, J.; Conn, C. E.; Mulet, X.; Waddington, L. J.; Drummond, C. J. Direct visualization of the structural transformation between the lyotropic liquid crystalline lamellar and bicontinuous cubic mesophase. *J. Phys. Chem. Lett.* **2018**, *9*, 3397-402. DOI PubMed
160. Van ’t Hag, N.; Gras, S. L.; Conn, C. E.; Drummond, C. J. Lyotropic liquid crystal engineering moving beyond binary compositional space - ordered nanostructured amphiphile self-assembly materials by design. *Chem. Soc. Rev.* **2017**, *46*, 2705-31. DOI PubMed
161. Gao, C.; Sakamoto, Y.; Sakamoto, K.; Terasaki, O.; Che, S. Synthesis and characterization of mesoporous silica AMS-10 with bicontinuous cubic $Pn\bar{3}m$ symmetry. *Angew. Chem. Int. Ed. Engl.* **2006**, *45*, 4295-8. DOI PubMed
162. Sorenson, G. P.; Schmitt, A. K.; Mahanthappa, M. K. Discovery of a tetracontinuous, aqueous lyotropic network phase with unusual 3D-hexagonal symmetry. *Soft Matter* **2014**, *10*, 8229-35. DOI PubMed
163. Angelopoulou, P. P.; Moutsios, I.; Manesi, G.; Ivanov, D. A.; Sakellariou, G.; Avgeropoulos, A. Designing high χ copolymer materials for nanotechnology applications: a systematic bulk *vs.* thin films approach. *Prog. Polym. Sci.* **2022**, *135*, 101625. DOI
164. Matsen, M. W.; Bates, F. S. Unifying weak- and strong-segregation block copolymer theories. *Macromolecules* **1996**, *29*, 1091-8. DOI
165. Leibler, L. Theory of microphase separation in block copolymers. *Macromolecules* **1980**, *13*, 1602-17. DOI
166. Olvera de la Cruz, M. Theory of microphase separation in block copolymer solutions. *J. Chem. Phys.* **1989**, *90*, 1995-2002. DOI
167. Bates, F. S.; Fredrickson, G. H. Block copolymer thermodynamics: theory and experiment. *Annu. Rev. Phys. Chem.* **1990**, *41*, 525-57. DOI PubMed

168. Zhang, B.; Zheng, C.; Bates, F. S.; Lodge, T. P. Self-assembly of charged diblock copolymers with reduced backbone polarity. *ACS Appl. Polym. Mater.* **2023**, *5*, 2223-9. DOI
169. Russell, S. T.; Bae, S.; Subramanian, A.; et al. Priming self-assembly pathways by stacking block copolymers. *Nat. Commun.* **2022**, *13*, 6947. DOI PubMed PMC
170. Bates, F. S.; Fredrickson, G. H. Block copolymers- designer soft materials. *Phys. Today* **1999**, *52*, 32-8. DOI
171. Wong, C. K.; Qiang, X.; Müller, A. H.; Gröschel, A. H. Self-assembly of block copolymers into internally ordered microparticles. *Prog. Polym. Sci.* **2020**, *102*, 101211. DOI
172. Khandpur, A. K.; Foerster, S.; Bates, F. S.; et al. Polyisoprene-polystyrene diblock copolymer phase diagram near the order-disorder transition. *Macromolecules* **1995**, *28*, 8796-806. DOI
173. Matsen, M. W.; Schick, M. Stable and unstable phases of a diblock copolymer melt. *Phys. Rev. Lett.* **1994**, *72*, 2660-3. DOI PubMed
174. Cochran, E. W.; Garcia-Cervera, C. J.; Fredrickson, G. H. Stability of the gyroid phase in diblock copolymers at strong segregation. *Macromolecules* **2006**, *39*, 2449-51. DOI
175. Hajduk, D. A.; Harper, P. E.; Gruner, S. M.; et al. The gyroid: a new equilibrium morphology in weakly segregated diblock copolymers. *Macromolecules* **1994**, *27*, 4063-75. DOI
176. Lai, C. T.; Shi, A. Binary blends of diblock copolymers: an effective route to novel bicontinuous phases. *Macromol. Theor. Simul.* **2021**, *30*, 2100019. DOI
177. Xie, O.; Cohen, A. E.; Bazant, M. Z.; Olsen, B. D. Learning nature's assembly language with polymers. *Proc. Natl. Acad. Sci. U. S. A.* **2026**, *123*, e2519094123. DOI PubMed PMC
178. Alward, D. B.; Kinning, D. J.; Thomas, E. L.; Fetters, L. J. Effect of arm number and arm molecular weight on the solid-state morphology of poly(styrene-isoprene) star block copolymers. *Macromolecules* **1986**, *19*, 215-24. DOI
179. Thomas, E. L.; Alward, D. B.; Kinning, D. J.; Martin, D. C.; Handlin, D. L.; Fetters, L. J. Ordered bicontinuous double-diamond structure of star block copolymers: a new equilibrium microdomain morphology. *Macromolecules* **1986**, *19*, 2197-202. DOI
180. Kinning, D. J.; Thomas, E. L.; Alward, D. B.; Fetters, L. J.; Handlin, D. L. Sharpness of the functionality-induced structural transition in poly(styrene-isoprene) star block copolymers. *Macromolecules* **1986**, *19*, 1288-90. DOI
181. Likhtman, A. E.; Semenov, A. N. Stability of the OBDD structure for diblock copolymer melts in the strong segregation limit. *Macromolecules* **1994**, *27*, 3103-6. DOI
182. Olmsted, P. D.; Milner, S. T. Strong-segregation theory of bicontinuous phases in block copolymers. *Phys. Rev. Lett.* **1995**, *74*, 829. DOI
183. Hajduk, D. A.; Harper, P. E.; Gruner, S. M.; Honeker, C. C.; Thomas, E. L.; Fetters, L. J. A reevaluation of bicontinuous cubic phases in starblock copolymers. *Macromolecules* **1995**, *28*, 2570-3. DOI
184. Susca, E. M.; Beaucage, P. A.; Thedford, R. P.; et al. Preparation of macroscopic block-copolymer-based gyroidal mesoscale single crystals by solvent evaporation. *Adv. Mater.* **2019**, *31*, e1902565. DOI
185. Lin, C.; Higuchi, T.; Chen, H.; Tsai, J.; Jinnai, H.; Hashimoto, T. Stabilizing the ordered bicontinuous double diamond structure of diblock copolymer by configurational regularity. *Macromolecules* **2018**, *51*, 4049-58. DOI
186. Chu, C.; Lin, W.; Tsai, J.; et al. Order-order transition between equilibrium ordered bicontinuous nanostructures of double diamond and double gyroid in stereoregular block copolymer. *Macromolecules* **2012**, *45*, 2471-7. DOI
187. Chu, C. Y.; Jiang, X.; Jinnai, H.; et al. Real-space evidence of the equilibrium ordered bicontinuous double diamond structure of a diblock copolymer. *Soft Matter* **2015**, *11*, 1871-6. DOI PubMed
188. Chu, C. Y.; Jiang, X.; Jinnai, H.; et al. Correction: real-space evidence of the equilibrium ordered bicontinuous double diamond structure of a diblock copolymer. *Soft Matter* **2015**, *11*, 4142. DOI PubMed
189. Winey, K. I.; Thomas, E. L.; Fetters, L. J. The ordered bicontinuous double-diamond morphology in diblock copolymer/homopolymer blends. *Macromolecules* **1992**, *25*, 422-8. DOI
190. Hsueh, H. Y.; Ling, Y. C.; Wang, H. F.; et al. Shifting networks to achieve subgroup symmetry properties. *Adv. Mater.* **2014**, *26*, 3225-9. DOI
191. An, T. H.; La, Y.; Cho, A.; et al. Solution self-assembly of block copolymers containing a branched hydrophilic block into inverse bicontinuous cubic mesophases. *ACS Nano* **2015**, *9*, 3084-96. DOI
192. Cho, A.; La, Y.; Shin, T. J.; Park, C.; Kim, K. T. Structural requirements of block copolymers for self-assembly into inverse bicontinuous cubic mesophases in solution. *Macromolecules* **2016**, *49*, 4510-9. DOI
193. La, Y.; An, T. H.; Shin, T. J.; Park, C.; Kim, K. T. A morphological transition of inverse mesophases of a branched-linear block copolymer guided by using cosolvents. *Angew. Chem. Int. Ed. Engl.* **2015**, *54*, 10483-7. DOI PubMed
194. Finnefrock, A. C.; Ulrich, R.; Du, Chesne. A.; et al. Metal oxide containing mesoporous silica with bicontinuous "plumber's nightmare" morphology from a block copolymer-hybrid mesophase. *Angew. Chem. Int. Ed.* **2001**, *40*, 1207-11. https://onlinelibrary.wiley.com/doi/abs/10.1002/1521-3773%2820010401%2940%3A7%3C1207%3A%3AAID-ANIE1207%3E3.0.CO%3B2-S.

195. Finnefrock, A. C.; Ulrich, R.; Toombes, G. E.; Gruner, S. M.; Wiesner, U. The plumber's nightmare: a new morphology in block copolymer-ceramic nanocomposites and mesoporous aluminosilicates. *J. Am. Chem. Soc.* **2003**, *125*, 13084-93. DOI PubMed

196. Toombes, G. E. S.; Finnefrock, A. C.; Tate, M. W.; Ulrich, R.; Wiesner, U.; Gruner, S. M. A re-evaluation of the morphology of a bicontinuous block copolymer-ceramic material. *Macromolecules* **2007**, *40*, 8974-82. DOI

197. Robbins, S. W.; Beaucage, P. A.; Sai, H.; et al. Block copolymer self-assembly-directed synthesis of mesoporous gyroidal superconductors. *Sci. Adv.* **2016**, *2*, e1501119. DOI PubMed PMC

198. Robbins, S. W.; Sai, H.; DiSalvo, F. J.; Gruner, S. M.; Wiesner, U. Monolithic gyroidal mesoporous mixed titanium-niobium nitrides. *ACS Nano* **2014**, *8*, 8217-23. DOI PubMed PMC

199. Cao, X.; Xu, D.; Yao, Y.; Han, L.; Terasaki, O.; Che, S. Interconversion of triply periodic constant mean curvature surface structures: from double diamond to single gyroid. *Chem. Mater.* **2016**, *28*, 3691-702. DOI

200. Bao, C.; Chen, H.; Che, S.; Han, L. Direct imaging of the structural transition and interconversion of macroporous bicontinuous diamond-surface structure. *Microporous Mesoporous Mater.* **2021**, *320*, 111084. DOI

201. Bao, C.; Che, S.; Han, L. Discovery of single gyroid structure in self-assembly of block copolymer with inorganic precursors. *J. Hazard. Mater.* **2021**, *402*, 123538. DOI PubMed

202. Matsen, M. W. Cylinder↔gyroid epitaxial transitions in complex polymeric liquids. *Phys. Rev. Lett.* **1998**, *80*, 4470-3. DOI

203. Sheng, Q.; Chen, H.; Mao, W.; Cui, C.; Che, S.; Han, L. Self-assembly of single-diamond-surface networks. *Angew. Chem. Int. Ed. Engl.* **2021**, *60*, 15236-42. DOI

204. Karpov, D.; Djeghdi, K.; Holler, M.; et al. High-resolution three-dimensional imaging of topological textures in nanoscale single-diamond networks. *Nat. Nanotechnol.* **2024**, *19*, 1499-506. DOI

205. Djeghdi, K.; Karpov, D.; Abdollahi, S. N.; et al. Block copolymer-directed single-diamond hybrid structures derived from X-ray nanotomography. *ACS Nano* **2024**, *18*, 26503-13. DOI PubMed PMC

206. Guillamat, P.; Mirza, W.; Bal, P. K.; et al. Guidance of cellular nematic elastomers into shape-programmable living surfaces. *Science* **2026**, *392*, 317-23. DOI

207. Wang, S.; Li, Y.; Yang, B.; et al. Evolution of curvatures between lamellar and bicontinuous phases: formation of saddle-shaped hierarchical lamellar structures in binary self-assembly system. *Small* **2026**, *22*, e08085. DOI

208. Wang, S.; Chen, H.; Zhong, T.; et al. Tetragonal gyroid structure from symmetry manipulation: a brand-new member of the gyroid surface family. *Chem* **2024**, *10*, 1406-24. DOI

209. Cui, C.; Cao, Y.; Han, L. Deep-learning-assisted understanding of the self-assembly of miktoarm star block copolymers. *ACS Nano* **2025**, *19*, 11427-39. DOI PubMed

210. Fronzi, M.; Stampfl, C.; Traversa, E. From atoms to systems: machine learning in the clean energy materials revolution. *Mater. Renew. Sustain. Energy* **2026**, *15*, 374. DOI

211. Saleh, G.; Manna, L. The predictive power of chemical bonding analysis in materials: a perspective on optoelectronic properties. *J. Am. Chem. Soc.* **2025**, *147*, 46705-19. DOI PubMed PMC

212. Shuang, F.; Wei, Z.; Liu, K.; Gao, W.; Dey, P. Universal machine learning interatomic potentials poised to supplant DFT in modeling general defects in metals and random alloys. *Mach. Learn.: Sci. Technol.* **2025**, *6*, 030501. DOI

213. Su, L.; Lu, F.; Li, Y.; et al. Gyroid liquid crystals as quasi-solid-state electrolytes toward ultrastable zinc batteries. *ACS Nano* **2024**, *18*, 7633-43. DOI

214. Tang, C.; Lu, W.; Zhang, Y.; et al. Toward ultrahigh rate and cycling performance of cathode materials of sodium ion battery by introducing a bicontinuous porous structure. *Adv. Mater.* **2024**, *36*, e2402005. DOI

215. Xiang, L.; Yuan, S.; Wang, F.; et al. Porous polymer cubosomes with ordered single primitive bicontinuous architecture and their sodium-iodine batteries. *J. Am. Chem. Soc.* **2022**, *144*, 15497-508. DOI

216. Reyes, C. F.; Ha, S.; Kim, K. T. Synthesis and applications of polymer cubosomes and hexosomes. *J. Polym. Sci.* **2023**, *61*, 1196-213. DOI

217. Li, Q.; Chen, C.; Li, C.; et al. Ordered bicontinuous mesoporous polymeric semiconductor photocatalyst. *ACS Nano* **2020**, *14*, 13652-62. DOI

218. Wang, C.; Lu, W.; Wang, J.; Che, S.; Lu, A.; Han, L. Synthesis of ordered mesoporous crystalline boron phosphate scaffold with double diamond surface structure. *Sci. China Chem.* **2025**, *68*, 590-600. DOI

219. Moore, W.; Shoji, S.; Tsaur, L.; et al. Asymmetric porous catalyst structures for low-temperature photocatalytic dry reforming of methane. *ACS Nano* **2025**, *19*, 23817-28. DOI

220. Cherevan, A. S.; Robbins, S.; Dieterle, D.; Gebhardt, P.; Wiesner, U.; Eder, D. Ordered gyroidal tantalum oxide photocatalysts: eliminating diffusion limitations and tuning surface barriers. *Nanoscale* **2016**, *8*, 16694-701. DOI PubMed

221. Li, W.; Ding, J.; Chen, X.; Wang, Y.; Song, X.; Zhang, S. A 3D-printed CuNi alloy catalyst with a triply periodic minimal surface for the reverse water-gas shift reaction. *J. Mater. Chem. A* **2023**, *12*, 314-20. DOI

222. Asmat, H.; Paul, P.; Mclaren, F.; et al. Electrified reformer for syngas production - additive manufacturing of coated microchannel monolithic reactor. *Appl. Catal. B Environ.* **2025**, *361*, 124640. DOI
223. Guo, Z. W.; Chen, C. C.; Huang, Y. T.; Fuh, Y. K. Self-powered fire alarm system based on $Ti_3C_2T_x$ MXene/PVP/piezoelectric fibers multilayers embedded with additively manufactured TPMS spacers with tunable stiffness. *Chem. Eng. J.* **2025**, *503*, 158423. DOI
224. Noroozi, R.; Quiquero, D.; Huang, Y. Y. S.; Shi, H. H. Hierarchical multi-material architectures with gradient design for dynamic-range flexible tactile sensing. *Adv. Mater. Technol.* **2026**, e02632. DOI
225. Pang, Y.; Zhu, X.; Liu, S.; Lee, C. A natural gradient biological-enabled multimodal triboelectric nanogenerator for driving safety monitoring. *ACS Nano* **2023**, *17*, 21878-92. DOI
226. Imanian, M. E.; Kardan-Halvaei, M.; Nasrollahi, F.; Imanian, A.; Montazerian, H.; Nasrollahi, V. 3D printed flexible wearable sensors based on triply periodic minimal surface structures for biomonitoring applications. *Smart Mater. Struct.* **2023**, *32*, 015015. DOI
227. Moeinnia, H.; Ganzert, C.; Schubert, L.; Kim, W. S. Streamlined custom manufacturing for optimized 3D printed prostheses through 3D pressure mapping. *Biosens. Bioelectron.* **2026**, *302*, 118560. DOI PubMed
228. Li, Z.; Feng, D.; Li, B.; et al. Ultra-wide range, high sensitivity piezoresistive sensor based on triple periodic minimum surface construction. *Small* **2023**, *19*, e2301378. DOI
229. Han, J.; Li, Z.; Kong, S.; Tang, S.; Feng, D.; Li, B. Wide-response-range and high-sensitivity piezoresistive sensors with triple periodic minimal surface (TPMS) structures for wearable human-computer interaction systems. *Compos. Part. B-Eng.* **2024**, *287*, 111840. DOI
230. Han, J.; Li, Z.; Kong, S.; et al. Enhanced sensitivity and broadband response in porous triple periodic minimal surface piezoresistive sensors for telemedicine applications. *Chem. Eng. J.* **2024**, *500*, 156989. DOI
231. Tang, C.; Zhu, J.; Wu, X.; Peng, Q.; Wang, X. Experimental investigation on multi-factor optimization of triply periodic minimal surface structured micro-generators via response surface methodology. *Energy* **2026**, *361*, 142181. DOI
232. Zhao, P.; Zhang, Y.; Qiao, Z. Research progress of 3D-printed anti-infective bone tissue engineering scaffolds based on triply periodic minimal surface structures. *APL Bioeng* **2026**, *10*, 021506. DOI PubMed PMC
233. Ramírez-Solana, D.; Sangiorgio, V.; Redondo, J.; Gulzari, M. Sound diffusion properties of triply periodic minimal surfaces using three-dimensional FDTD simulations. *Appl. Math. Model.* **2026**, *157*, 116867. DOI
234. Roohani, I.; Entezari, A.; Zreiqat, H. Liquid crystal display technique (LCD) for high resolution 3D printing of triply periodic minimal surface lattices bioceramics. *Addit. Manuf.* **2023**, *74*, 103720. DOI
235. Papkov, V.; Tartakovsky, L.; Pashchenko, D. Triply periodic minimal surfaces as catalyst carriers of compact reformers for hydrogen production and storage systems: recent advances and future perspectives. *Renew. Sustain. Energy Rev.* **2026**, *237*, 117070. DOI
236. Karami, Z.; Hamidi, M. Cubosomes: remarkable drug delivery potential. *Drug Discov. Today* **2016**, *21*, 789-801. DOI PubMed
237. Hur, K.; Hennig, R. G.; Wiesner, U. Exploring periodic bicontinuous cubic network structures with complete phononic bandgaps. *J. Phys. Chem. C* **2017**, *121*, 22347-52. DOI
238. Flavell, W.; Neophytou, A.; Demetriadou, A.; Albrecht, T.; Chakrabarti, D. Programmed self-assembly of single colloidal gyroids for chiral photonic crystals. *Adv. Mater.* **2023**, *35*, e2211197. DOI PubMed
239. Liu, Y.; Zhou, Q.; Yu, H.; et al. Increasing the accessibility of internal catalytic sites in covalent organic frameworks by introducing a bicontinuous mesostructure. *Angew. Chem. Int. Ed. Engl.* **2024**, *63*, e202400985. DOI
240. Li, C.; Pan, Y.; Xiao, T.; et al. Metal organic framework cubosomes. *Angew. Chem. Int. Ed. Engl.* **2023**, *62*, e202215985. DOI
241. Zhang, Y.; Zhang, J.; Yang, W.; Che, S.; Cao, Y.; Han, L. Chirality manipulation of 3D printed gyroidal scaffolds towards mechanical properties enhancement. *Addit. Manuf.* **2024**, *96*, 104551. DOI
242. Zhang, Y.; Zhang, J.; Chen, X.; et al. Mechanical properties of 3D-printed polymeric cellular structures based on bifurcating triply periodic minimal surfaces. *Adv. Eng. Mater.* **2025**, *27*, 2402507. DOI
243. Zhang, Y.; Zhang, J.; Zhao, X.; et al. Mechanical behaviors regulation of triply periodic minimal surface structures with crystal twinning. *Addit. Manuf.* **2022**, *58*, 103036. DOI
244. Tang, C.; Zhang, W.; Zhang, Y.; et al. Bicontinuous structure mediated microstructural engineering of hard carbon for enhanced sodium storage. *Adv. Mater.* **2026**, *38*, e11632. DOI
245. Liu, C.; Yoshio, M. Topology-controlled proton transport in thermotropic liquid-crystalline acid-base complexes. *Chem. Mater.* **2026**, *38*, 10106-17. DOI
246. Jennings, J.; Pabst, G. Multiple routes to bicontinuous cubic liquid crystal phases discovered by high-throughput self-assembly screening of multi-tail lipidoids. *Small* **2023**, *19*, e2206747. DOI PubMed
247. Chen, Z.; Huang, Q.; Song, Y.; et al. Cubosomes-assisted transdermal delivery of doxorubicin and indocyanine green for chemo-photothermal combination therapy of melanoma. *Biomed. Pharmacother.* **2023**, *166*, 115316. DOI
248. Kibsgaard, J.; Chen, Z.; Reinecke, B. N.; Jaramillo, T. F. Engineering the surface structure of MoS_2 to preferentially expose active edge sites for electrocatalysis. *Nat. Mater.* **2012**, *11*, 963-9. DOI PubMed

249. Morey, M.; Davidson, A.; Stucky, G. Silica-based, cubic mesostructures: synthesis, characterization and relevance for catalysis. *J. Porous Mater.* **1998**, *5*, 195-204. DOI
250. Niu, T.; Li, R.; Chen, X.; et al. Revealing the underlying mechanisms in performance enhancement of shellular lattice electrodes during anion exchange membrane water electrolysis process. *Adv. Sci. (Weinh).* **2026**, e77317. DOI PubMed PMC
251. Liao, N.; Zhao, J.; Luo, J. 3D-printed metal electrodes with enhanced bubble removal for efficient water electrolysis. *Nano Lett.* **2025**, *25*, 9551-9. DOI PubMed
252. Crossland, E. J.; Kamperman, M.; Nedelcu, M.; et al. A bicontinuous double gyroid hybrid solar cell. *Nano Lett.* **2009**, *9*, 2807-12. DOI
253. Li, Y.; Zhang, M.; Xu, Z.; et al. Biomimetic porous carbon of marine sponge for high performance cathode of Li-S battery. *Adv. Mater.* **2026**, *38*, e73073. DOI
254. Werner, J. G.; Rodríguez-Calero, G. G.; Abruña, H. D.; Wiesner, U. Block copolymer derived 3-D interpenetrating multifunctional gyroidal nanohybrids for electrical energy storage. *Energy. Environ. Sci.* **2018**, *11*, 1261-70. DOI
255. Zhou, Z.; Lalwani, A. R.; Sun, X.; et al. Monolithic gyroidal solid oxide cells by additive manufacturing. *Nat. Energy* **2025**, *10*, 962-70. DOI
256. Xie, W.; Huang, X.; Zhu, C.; et al. A versatile synthesis platform based on polymer cubosomes for a library of highly ordered nanoporous metal oxides particles. *Adv. Mater.* **2024**, *36*, e2313920. DOI
257. Alzoubi, M. A.; Al-Ketan, O.; Muthusamy, J.; Sasmito, A. P.; Poncet, S. Mixing performance of T-shape micromixers equipped with 3D printed gyroid matrices: a numerical evaluation. *Results Eng.* **2023**, *17*, 100811. DOI
258. Tang, W.; Zhou, H.; Zeng, Y.; et al. Analysis on the convective heat transfer process and performance evaluation of triply periodic minimal surface (TPMS) based on diamond, gyroid and Iwp. *Int. J. Heat Mass Transfer.* **2023**, *201*, 123642. DOI
259. Wang, H.; Zheng, S.; Liu, G.; et al. Influences of the flow rate and fluid volume in air-kerosene cross-flow heat exchangers using gyroid-typed triply periodic minimal surfaces. *Appl. Therm. Eng.* **2025**, *263*, 125336. DOI
260. Wang, H.; Zhao, C.; Liu, W.; Liu, Z.; Bian, H.; Zhang, K. Advances in triply periodic minimal surface structures for thermal management systems: A comprehensive review. *Appl. Therm. Eng.* **2025**, *279*, 127481. DOI
261. Zhao, R.; Yuan, K.; Deng, J.; et al. Enhanced hydrogen storage performance by incorporating triply periodic minimal surface into metal hydride reactor. *Renew. Energy* **2026**, *270*, 125896. DOI
262. Chen, J.; Liu, X.; Li, Y.; et al. Numerical and experimental investigation of TPMS-structured cold plates for electronic device cooling. *Appl. Energy* **2025**, *401*, 126745. DOI
263. Li, S.; Zhang, H.; Ma, S.; et al. Fundamentals, classification of photonic crystals and their applications in textiles: a review. *Adv. Fiber Mater.* **2026**, *8*, 1759-803. DOI
264. Meng, Z.; Miao, S.; Liu, Y.; et al. Photonic crystal-based structural color switches. *Mater. Horiz.* **2025**, *12*, 8380-408. DOI
265. Li, P.; Wu, J.; Chen, K.; Dong, J.; Hu, Y. Advances in the fabrication of multiple stopband photonic crystal microparticles. *CrystEngComm* **2025**, *27*, 4796-809. DOI
266. Lv, J.; Gao, X.; Tang, Z. Bioinspired chiral photonic crystals. *Sci. China Mater.* **2025**, *68*, 979-97. DOI
267. Dolan, J. A.; Wilts, B. D.; Vignolini, S.; Baumberg, J. J.; Steiner, U.; Wilkinson, T. D. Optical properties of gyroid structured materials: from photonic crystals to metamaterials. *Adv. Opt. Mater.* **2015**, *3*, 12-32. DOI
268. Zhang, W.; Min, J.; Wang, H.; et al. Printing of 3D photonic crystals in titania with complete bandgap across the visible spectrum. *Nat. Nanotechnol.* **2024**, *19*, 1813-20. DOI
269. Jo, S.; Park, H.; Lee, J.; et al. Visible photonic bandgap configured by non-affine block copolymer gyroid. *Adv. Opt. Mater.* **2026**, *14*, e02817. DOI
270. Vignolini, S.; Yufa, N. A.; Cunha, P. S.; et al. A 3D optical metamaterial made by self-assembly. *Adv. Mater.* **2012**, *24*, OP23-7. DOI
271. Park, H.; Jo, S.; Kang, B.; et al. Block copolymer gyroids for nanophotonics: significance of lattice transformations. *Nanophotonics* **2022**, *11*, 2583-615. DOI PubMed PMC
272. Lu, L.; Joannopoulos, J. D.; Soljačić, M. Topological photonics. *Nat. Photon.* **2014**, *8*, 821-9. DOI
273. Lu, L.; Fu, L.; Joannopoulos, J. D.; Soljačić, M. Weyl points and line nodes in gyroid photonic crystals. *Nat. Photon.* **2013**, *7*, 294-9. DOI
274. Fang, C.; Lu, L.; Liu, J.; Fu, L. Topological semimetals with helicoid surface states. *Nat. Phys.* **2016**, *12*, 936-41. DOI
275. Lu, L.; Wang, Z.; Ye, D.; et al. TOPOLOGICAL MATTER. Experimental observation of Weyl points. *Science* **2015**, *349*, 622-4. DOI
276. Liu, B.; Johnson, S. G.; Joannopoulos, J. D.; Lu, L. Generalized gilat-raubenheimer method for density-of-states calculation in photonic crystals. *J. Opt.* **2018**, *20*, 044005. DOI
277. Lu, L.; Gao, H.; Wang, Z. Topological one-way fiber of second Chern number. *Nat. Commun.* **2018**, *9*, 5384. DOI PubMed PMC
278. Watanabe, H.; Lu, L. Space group theory of photonic bands. *Phys. Rev. Lett.* **2018**, *121*, 263903. DOI PubMed
279. Kim, H.; Cheng, H.; Lu, L.; Murakami, S. Theoretical analysis of glide-Z_2 magnetic topological photonic crystals. *Opt. Express* **2021**, *29*, 31164-78. DOI

280. Sam, S.; Say, S.; Sang, L.; Nakatsugawa, H. Nanostructuring thermoelectric materials using phononic crystals and reduction in lattice thermal conductivity. *Next Energy* **2026**, *11*, 100550. DOI
281. Guo, L.; Zhao, S.; Guo, Z.; Zhang, Y.; Yang, J.; Kitipornchai, S. Phase transition-based tunable phononic crystals and metamaterials: a review. *Thin-Walled Struct.* **2026**, *218*, 113984. DOI
282. Bahrami, A.; Motaei, F. A review of phononic-crystal-based energy harvesters. *Prog. Energy* **2025**, *7*, 012002. DOI
283. Wu, B.; Jiang, W.; Jiang, J.; et al. Wave manipulation in intelligent metamaterials: recent progress and prospects. *Adv. Funct. Mater.* **2024**, *34*, 2316745. DOI
284. He, Y.; Wu, Y.; Qin, Y.; et al. Research on the control method of Bragg bandgap characteristics of phononic crystal beams based on Cantor fractals. *J. Phys. D: Appl. Phys.* **2026**, *59*, 015301. DOI
285. Wang, Y.; Li, D. Design of a defect containing bi-material nested structure phononic crystal with adjustable band gap. *Appl. Acoust.* **2025**, *240*, 110930. DOI
286. Chen, Y.; Liang, S.; Lan, Z.; Gu, Z.; Su, Z.; Zhu, J. A triply periodic minimal surface-based acoustic crystal with double-zero index. *Mater. Horiz.* **2026**, *13*, 6428-33. DOI
287. Wu, Y.; Qi, X.; Sun, L.; Wang, B.; Wang, P.; Li, W. Acoustic performance of micro-perforated plate sandwich structure based on triply periodic minimal surfaces. *Mater. Today Commun.* **2025**, *49*, 114249. DOI
288. Chen, X.; Sun, G.; Zhu, J.; Kang, W.; Shang, D.; Deng, Z. Influence of structural parameters on mechanical properties of triply periodic minimal surface structure. *Metals* **2023**, *13*, 285. DOI
289. Chatzigeorgiou, C.; Piotrowski, B.; Chemisky, Y.; Laheurte, P.; Meraghni, F. Numerical investigation of the effective mechanical properties and local stress distributions of TPMS-based and strut-based lattices for biomedical applications. *J. Mech. Behav. Biomed. Mater.* **2022**, *126*, 105025. DOI PubMed
290. Barber, H.; Kelly, C. N.; Nelson, K.; Gall, K. Compressive anisotropy of sheet and strut based porous Ti-6Al-4V scaffolds. *J. Mech. Behav. Biomed. Mater.* **2021**, *115*, 104243. DOI PubMed
291. Zhang, L.; Feih, S.; Daynes, S.; et al. Energy absorption characteristics of metallic triply periodic minimal surface sheet structures under compressive loading. *Addit. Manuf.* **2018**, *23*, 505-15. DOI
292. Vijayavenkataraman, S.; Zhang, L.; Zhang, S.; Fuh, J. Y. H.; Lu, W. Triply periodic minimal surfaces sheet scaffolds for tissue engineering applications: an optimization approach toward biomimetic scaffold design. *ACS Appl. Bio. Mater.* **2018**, *1*, 259-69. DOI
293. Al-Ketan, O.; Rowshan, R.; Abu Al-Rub, R. K. Topology-mechanical property relationship of 3D printed strut, skeletal, and sheet based periodic metallic cellular materials. *Addit. Manuf.* **2018**, *19*, 167-83. DOI
294. Maskery, I.; Aboulkhair, N.; Aremu, A.; Tuck, C.; Ashcroft, I. Compressive failure modes and energy absorption in additively manufactured double gyroid lattices. *Addit. Manuf.* **2017**, *16*, 24-9. DOI
295. Sajadi, S. M.; Owuor, P. S.; Schara, S.; et al. Multiscale geometric design principles applied to 3D printed schwarzites. *Adv. Mater.* **2018**, *30*, 1704820. DOI

Disclaimer/Publisher's Note: All statements, opinions, and data contained in this publication are solely those of the individual author(s) and contributor(s) and do not necessarily reflect those of OAE and/or the editor(s). OAE and/or the editor(s) disclaim any responsibility for harm to persons or property resulting from the use of any ideas, methods, instructions, or products mentioned in the content.


© The Author(s) 2026. Open Access This article is licensed under a Creative Commons Attribution 4.0 International License (https://creativecommons.org/licenses/by/4.0/), which permits unrestricted use, sharing, adaptation, distribution and reproduction in any medium or format, for any purpose, even commercially, as long as you give appropriate credit to the original author(s) and the source, provide a link to the Creative Commons license, and indicate if changes were made.